Dispersion Curve Estimation for Longitudinal Rail Stress Measurement

Nicholas A. Corbin

Thesis submitted to the Faculty of the
Virginia Polytechnic Institute and State University
in partial fulfillment of the requirements for the degree of

Master of Science
in
Engineering Mechanics

Pablo A. Tarazaga, Chair
Shane D. Ross
John P. Domann

July 9, 2021
Blacksburg, Virginia

Keywords: Non-destructive evaluation, dispersion curve, spectrum relation, stress measurement, wave propagation, rail neutral temperature

Copyright 2021, Nicholas A. Corbin

Dispersion Curve Estimation for Longitudinal Rail Stress Measurement

Nicholas A. Corbin

(ABSTRACT)

There currently exists no reliable, non-destructive method for measuring stress in railroads and other similar structures without the need for a calibration measurement. Major limitations which have hindered previous techniques include sensitivity to boundary conditions, insensitivity to stress, and intolerance for material and geometry uncertainty. In this work, a technique is developed which seeks to solve these challenges by extracting the spectrum relation, or dispersion curve, of a waveguide from dispersive wave propagation meaasurements. The technique is based on spectral analysis of waves in structures modeled as beams, and as such is based on relatively low frequency vibrations, as opposed to other techniques which use nonlinear elastic modeling of structures at ultrasonic frequencies. The major contribution of this work is the development of a frequency-domain based signal processing technique which is capable of compensating for the dispersive, long wavelength reflections which have limited the ability of previous techniques to go low enough in frequency to achieve high stress sensitivity. By compensating for reflections, the present work is able to automate the process of analyzing wave propagation signals such that the entire dispersion curve can be extracted, enabling the identification of various parameters including stress, stiffness, density, and other material and geometry properties. This in turn enables measuring stress, performing model-updating for material and geometry uncertainty, and being indifferent to boundary conditions. The theory and algorithmic implementation is presented, along with simulations and experimental validation on a rectangular beam.

Dispersion Curve Estimation for Longitudinal Rail Stress Measurement

Nicholas A. Corbin

(GENERAL AUDIENCE ABSTRACT)

The ability to detect damage or the potential for damage in structures is highly desirable, especially in industries such as civil infrastructure in which failure can be incredibly costly and dangerous. In particular, non-destructive techniques which can predict failure without interfering with the operations of a structure are particularly sought after. In this work, a technique for non-intrusively and non-destructively measuring stress is developed, with the primary application being for measuring stress in railroads. The technique seeks to advance the state-of-the-art in wave-propagation-based techniques by adding the capability to automatically identify reflected waves. With this new capability, the method is able to quickly and efficiently analyze a large set of vibration measurements to extract information about the structure's material, geometry, and loading characteristics which enables solving for stress even when the structures material, geometry, and boundary conditions are not precisely known. The technique is demonstrated on both simulated and experimental data, in which a rectangular beam is tensioned and the stress is then identified.

Dedication

For my parents

Acknowledgments

I would like to sincerely thank Dr. Pablo Tarazaga, for providing guidance and believing in me even when I didn't believe in myself. As an advisor, mentor, and friend, Dr. Tarazaga gave me the environment and support to succeed and to find my place in graduate school. I would also like to thank my lab mates, with whom I have had many interesting and stimulating discussions. Despite being one of the newest members of the lab, I was immediately welcomed and encouraged to speak up and participate in discussions, and I learned so much from interacting with them.

I would also like to thank my committee members, Dr. John Domann and Dr. Shane Ross, for their feedback, discussions, and insights about the fundamentals. Special thanks to Dr. Domann regarding a very helpful discussion about the appearance of geometric nonlinearity due to the inclusion of prestress in my model, and special thanks to Dr. Ross for guidance during my PhD program applications.

Finally, I would like to thank my friends and family; without them, I would never have made it this far.

Nicholas A. Corbin

Blacksburg, VA, USA. July 2021.

Contents

List of Figures

List of Tables

List of Abbreviations

α Coefficient of thermal expansion

Δx A change in position along the structure

$\hat{U}_n$, $\hat{A}_n$, $\hat{B}_n$, … Amplitude spectrum

$\hat{u}_n(x)$ The n^{th} Fourier coefficient

κ Timmoshenko correction factor

ν Poisson ratio

ω Angular frequency, in rad./s

$\psi(x,t)$ the rotation ψ of a beam's cross-section at location x and time t

ρ Density

σ Longitudinal stress

A Cross-section area

E Elastic modulus, i.e. stiffness or Young's modulus

E Elastic modulus

F_0 Axial force

G Shear modulus

$G(k_n x)$ Phase spectrum

I Second moment of area, i.e. cross-section's area moment of inertia

k Angular wavenumber, in rad./m

M Bending moment

T Temperature

T_0 Neutral temperature

$u(x,t)$ the deflection u of a beam at location x and time t

V Shear force

w Weighting

CFT Continuous Fourier Transform

CWR Continuously Welded Rail

DFT Discrete Fourier Transform

FFT Fast Fourier Transform

FRA Federal Railroad Administration

IEPE Integrated Electronic Piezoelectric

MFC Macro-Fiber Composite (a type of piezoelectric actuator)

NDE Non-Destructive Evaluation

PSD Power Spectral Density

RNT Rail Neutral Temperature

SHM Structural Health Monitoring

SNR Signal-to Noise Ratio

SSP Split-Spectrum Processing

Chapter 1

Introduction

1.1 Background and motivation

Structural health monitoring (SHM) is a field concerned with detecting damage or the potential for failure in structures under operation. Monitoring structures while they are in-use and without interrupting operation presents a challenge, as the level of control and certainty available in lab-based testing is often unavailable for structures in operation. This is because many traditional evaluation methods, such as material tensile testing or impact testing, are destructive in nature, often requiring cutting a sample from a structure or permanently damaging a test article. There is therefore a high demand for non-destructive evaluation (NDE) methods, which are unique in their ability to characterize a structure's damage in a non-invasive manner.

According to Farrar and Worden [14], damage can be defined as a change which may inhibit the current or future performance of a system. The extent to which damage is tolerated varies between applications, and in some fields, such as aerospace, mechanical, and civil engineering, significant effort is expended to produce damage tolerant designs. Nonetheless, there are still countless examples of systems in which the designed damage tolerance was insufficient to prevent catastrophic failure. Thus, while many SHM techniques seek to detect or localize damage once it has occurred, SHM can also be concerned with detecting damage before it happens.

As a supplement to damage tolerant design, the ability to monitor the stress of structures during operation could provide a warning to avoid critical failures. Motivated by this problem, this thesis seeks to develop a non-destructive and minimally invasive technique for measuring stress in-situ in structures.

1.1.1 Rail neutral temperature and longitudinal rail stress

Modern railroads are constructed using continuously welded rail (CWR) consisting of prefabricated sections of rail (typically about 400 feet long [32]) that are welded together to form a continuous track. Eliminating the gaps between rail sections by welding them together in this manner allows trains to travel with fewer vibrations, enabling them to travel at higher speeds, providing a smoother ride, and reducing associated maintenance costs. However, without gaps to accommodate expansion and contraction due to temperature changes, CWR becomes more susceptible to buckling or cracking. During periods of high heat, CWR experiences a buildup of compressive stresses, whereas during periods of intense cold, CWR can experience intense tension; in both cases, the extreme stress can cause problems (see Fig. 1.1).

Track buckling in particular represents a major challenge for the rail industry. Repairing a buckled track is costly and time consuming, and the losses due to halted train traffic can be major. The most critical damage, however, occurs if a train happens to be on the track at the time of buckling: trains are often derailed, resulting in damages to the train, cargo, and potential loss of life. In 1977, the Federal Rail Administration reported 109 train derailments due to buckling, and by 1982 annual derailments had risen to almost 175 [21]. In the following decades, with improved maintenance procedures and stricter traffic policies, the industry was able to reduce the number to 34 derailments per year by the early

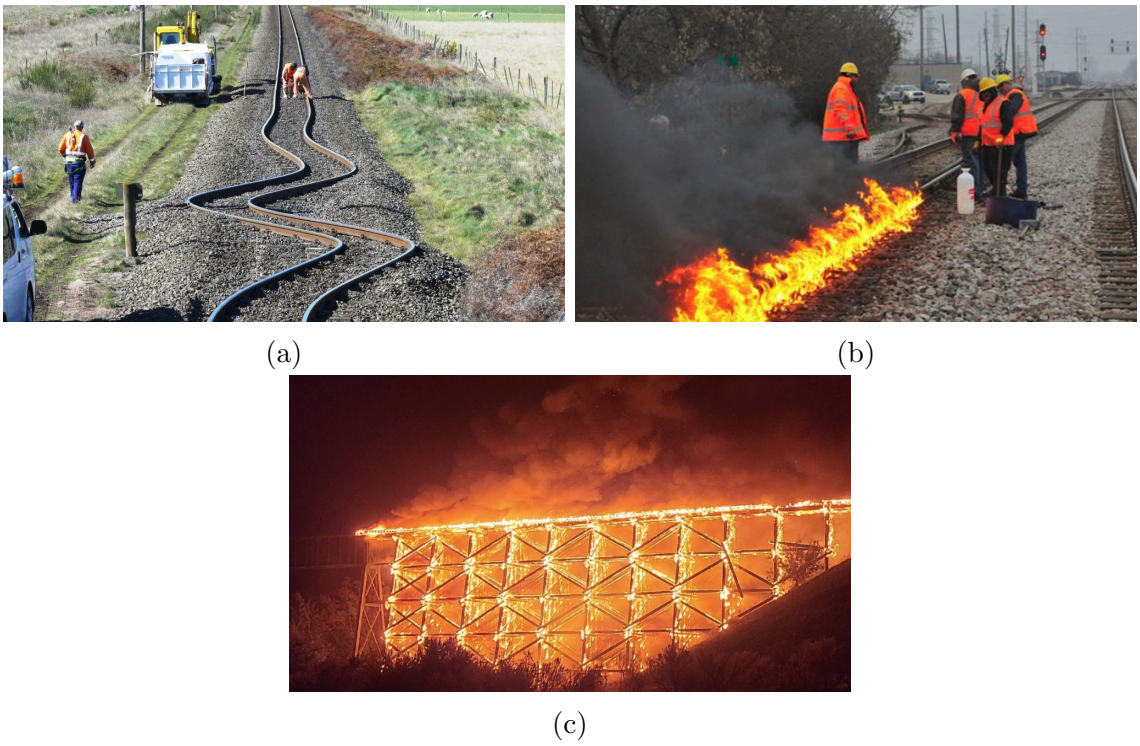

(a) (b)

(c)

Figure 1.1: Images showing (a) dramatic buckling of a rail due to thermal expansion (reproduced from [41]), (b) a rail which has been intentionally set on fire to prevent cracking due to shrinkage (reproduced from [10]), and (c) a rail bridge which has not intentionally been set on fire (reproduced from [43]).

2000s. However, the economic impacts of derailment continued to rise despite the decrease in derailment events (likely due to higher train speeds and more valuable cargo) such that the damages peaked at $17 million by 2002 [24].

As rail infrastructure continues to grow to match increasing demand, there is more rail to monitor and more opportunity for damage. With no current method for actively monitoring all of the rail, the rail industry must impose broad safety measures across the board such as lowering train speeds or altogether halting traffic on particularly hot days when buckling is likely to occur. According to a study funded by the Environmental Protection Agency, the rail industry is projected to lose on the order of $70 billion by the year 2100 due to these policies alone. However, the study predicted that losses by the year 2100 could be as high

as $138 billion due the rise in global temperatures on average due to climate change [9].

In order to avoid such losses, it is necessary to minimize the opportunity for extreme rail stresses by setting the Rail Neutral Temperature (RNT) — i.e., the temperature at which the rail is in equilibrium — appropriately between the highest and lowest anticipated temperatures which the section of rail may experience during its operation. The RNT can be prescribed by tensioning the rail to an appropriate value using a tensioner or heating the rail artificially during the installation process using a heater, as shown in Fig. 1.2, or simply by installing the rail when the ambient temperature is appropriate. For this reason, new rail is typically installed in the summer. However, expansion and contraction due to thermal stresses, vibrations due to train traffic, and shifting of the underlying ground over time can cause the RNT to shift, exacerbating the possibility for rail buckling or fracture due to extreme stress. Therefore, RNT must regularly be monitored in order to ensure that the expected rail temperatures do not result in excessive stresses.

(a) A hydraulic rail tensioner. (b) A propane rail heater.

Figure 1.2: Tools for setting the RNT during track installation (reproduced from [15]).

Monitoring RNT involves measuring or calculating the temperature at which the rail experiences a neutral stress state. As has been alluded to, the main source of stress in rails is thermal stress due to constrained thermal expansion [25]. Note that in the absence of

boundaries, i.e. for an unconstrained rail, the rail could experience temperature changes with *no* change in stress; thermal stress is really a mechanical stress induced by constraining the rail when it would otherwise seek to lengthen or shorten. In such a case, the total longitudinal strain of the structure ε_x is zero because the eigenstrain induced by thermal expansion is negated by the mechanical strain resulting from the mechanical stress from the forces constraining the rail[1]. The relationship between temperature and longitudinal stress in the case of a worst-case, perfectly constrained rail is given by Eq. (1.1)

$$\sigma = -E\alpha\Delta T, \tag{1.1}$$

where σ represents the longitudinal rail stress (negative for compression), E is the elastic modulus, α is the coefficient of thermal expansion, and $\Delta T = T - T_0$ is the temperature above the rail neutral temperature [1]. For a rail with known material properties E and α, a single measurement of stress σ at a particular temperature T is sufficient to solve for RNT by rearranging Eq. (1.1):

$$T_0 = \frac{\sigma + E\alpha T}{E\alpha}.$$

Fig. 1.3a shows how a single measurement of stress and temperature, along with the coefficient of thermal expansion, can be used to find the neutral temperature via linear regression, as shown in Fig. 1.3b. In practice, multiple measurements may be taken at different stress/temperature conditions in order to obtain a least-squares estimate of the RNT to accommodate measurement uncertainty.

[1] This assumes the worst-case scenario where the rail is completely constrained in the longitudinal direction; some locations, such as near a curved section of track, may have some ability to expand and contract, resulting in a non-zero longitudinal strain ε_x, in which case the corresponding stress would be given by $\sigma = -E(\alpha\Delta T - \varepsilon_x)$ [1].

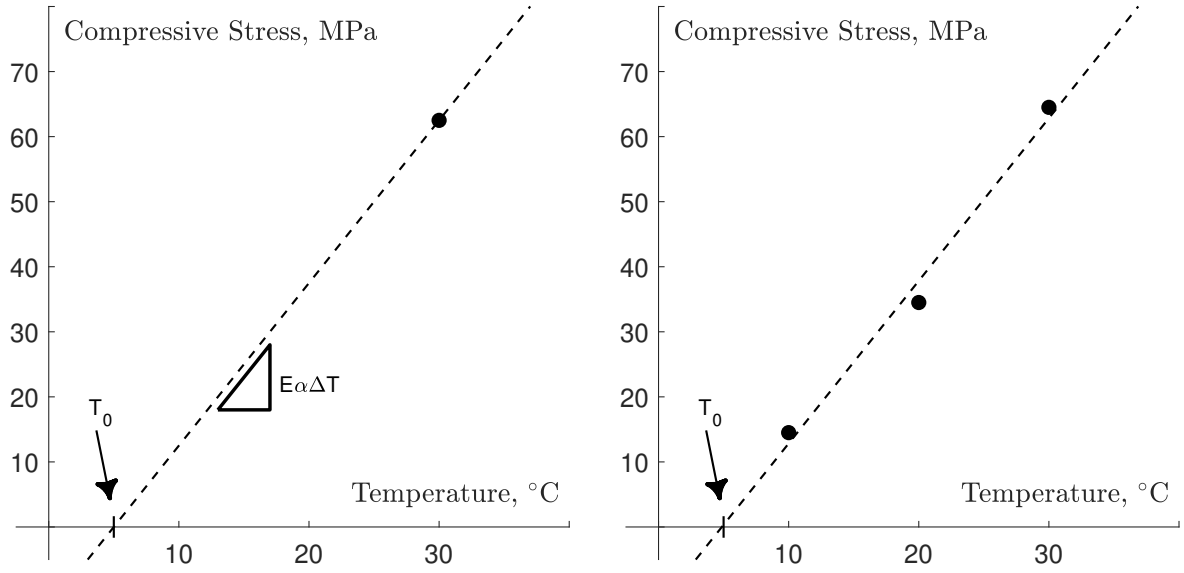

(a) Exact linear fit. (b) Least-squares linear fit.

Figure 1.3: The linear relationship between thermal stress and temperature, according to Eq. (1.1).

Thus, the process for monitoring RNT generally requires measuring the longitudinal rail stress and the corresponding temperature. Temperature measurements can be obtained rather easily using a magnetic thermometer or thermocouple attached to the rail. However, the task of measuring absolute stress is not as straightforward. Typically, stress in structures is calculated by measuring strain using a strain gage, and then using a constitutive relationship (i.e., Hooke's law) to calculate the corresponding stress. This method is only suitable for measuring relative stress, i.e., the difference between the current stress and the stress at the time of applying the strain gage, which may not be known. Furthermore, strain gages only measure mechanical strain; in structures experiencing constrained thermal expansion though, the structure experiences a buildup of stress *without* a corresponding mechanical strain. To account for these limitations, measuring stress in CWR with a strain gage requires cutting the rail. With the rail free to relax, a strain gage can then be applied to the rail in a known neutral state, the rail must be re-tensioned and re-welded, and then the strain measurement will correspond to the true stress value. This method is destructive,

costly, and time consuming; nonetheless, it is still the standard and most reliable method for measuring stress in rails. For these reasons, a NDE technique for measuring stress is highly sought after in the rail maintenance community.

1.2 Review of literature

In the following section, a review of the relevant literature used in this thesis is presented. The literature falls into three main categories, characterized by the different communities from which the literature is taken. First, an overview of the prior NDE techniques for measuring stress in rails is presented, culminating in the work of Albakri et al. [3] which served as the foundation for this thesis. This body of literature contains the prior work relevant to the direct application of this thesis work. Next, a review is provided of signal processing techniques for compensating for random and coherent noise. Noise presented a major challenge for the proposed technique, so a significant amount of effort was exerted to find solutions developed already by the academic community; in this case, the radar literature served as a major collection of useful signal processing techniques. Finally, while stress measurement is the motivation of this work, the fundamental nature of the techniques described herein relates to measuring the spectrum relation, or the dispersion curve, for a system. As such, a review of literature relating to dispersion curve measurement techniques is also provided.

1.2.1 Prior NDE stress measurement techniques

The development of an alternative to the current expensive, time consuming, and destructive techniques for measuring stress in rails has been highly sought after for decades [21]. In

fact, a non-destructive stress measurement system "is commonly considered the 'Holy Grail' of railway maintenance today" [34]. Recognizing the importance of such a measurement system, in 1982, the Federal Railroad Administration (FRA) formed a committee with the National Academy of Sciences to review the topic of longitudinal rail stress and to develop short, medium, and long-term recommendations. The report published by the committee identified the following requirements for a successful NDE stress measurement tool [21]:

1. Rugged
2. Easy to use
3. Nondestructive
4. No disturbance to track
5. No calibration needed
6. Independent of size, wear, etc.; independent of material microstructure
7. No surface preparation required
8. Measures absolute force
9. No permanent attachment needed
10. Provides continuous measurement
11. Compatible with temperature measurement

Items 4, 5, 6, and 8 have turned out to be some of the major challenges; that is, disturbances to the track's clamping conditions or calibration procedures are often required to obtain an accurate absolute stress measurement because techniques to-date are too sensitive to material/geometry variations and in-field boundary condition variability. The remainder of this section will provide a brief overview of existing NDE stress measurement techniques, along with an explanation of why the techniques have not been adopted by the rail maintenance community.

For some brief context, some of the different techniques based on vibrations use signals with drastically different frequency ranges. Characteristic lengths associated with the rail structure include the thickness of the rail and the spacing of cross-ties on which the rail sits. Ultrasonic techniques use frequencies for which the wavelength is much shorter than the cross-tie distance or even the rail thickness, and as such can be categorized as 'high frequency' techniques. These techniques require more complex modeling, as elementary beam assumptions are not valid in the ultrasonic response range. As such, since elementary beam theory assumptions are more admissible for lower frequencies, techniques which permit the use of elementary beam theories will be referred to as low frequency, whereas techniques such as ultrasonic techniques where elementary beam assumptions break down will be referred to as high frequency.s

Acoustoelastic Ultrasonic Wave Propagation

Ultrasonic testing has been a successful NDE technique with a wide variety of applications, including damage localization and material characterization. This success has encouraged researchers to investigate other applications as well, one of popular interest being non-destructive stress measurement. Ultrasonic stress measurement techniques are generally built upon the non-linear theory of elasticity developed by Murnaghan [33] in 1937. Hughes and Kelly [20] in 1953 derived expressions for the velocities of elastic waves in stressed solids based upon Murnaghan's theory, establishing the field of acoustoelasticity. Egle and Bray [13] in 1976 then presented the first measurements of the stress-induced changes in ultrasonic wave speeds in rail steels, validating the theory for use in rail applications.

The general approach of ultrasonic stress measurement is to use two ultrasonic transducers in a pitch-catch configuration a distance Δx apart from each other, and to measure time-of-flight Δt for pulses traveling from one transducer to the other. The phase or group velocity

for the pulse can then be estimated as $v = \frac{\Delta x}{\Delta t}$, depending on the criteria for defining the time-of-flight Δt. Since the waves of interest are dispersive, both the phase and group velocity are frequency dependent; thus, the *frequency* for a measured velocity should always be specified.

In practice [40], some heuristics are often employed 1) in the criteria for the time-of-flight, and 2) in selecting the frequency to which the velocity corresponds (be it phase or group velocity). In particular, since the waves are dispersive, the peaks and valleys shift and the wave "spreads out" as the wave propagates, making it difficult to pick a consistent feature on the wave at both measurement locations in order to define the time-of-flight. One could attempt to track a single peak, which would travel at *a* phase velocity, but the question of what the corresponding frequency for the measured phase velocity should be arises. Similarly, one could draw an envelope over the wave packet and track the peak of the envelope, which would relate to *a* group velocity; again, the question arises as to the appropriate frequency to assign the group velocity. In both cases, authors presumably take the center frequency of the pulse to answer these questions (though it is not explicitly stated). Another method involves using combined time-frequency analysis, such as by using a wavelet transform. This method still gives a single wave velocity for a pulse consisting of a range of frequencies.

The major limitation of acoustoelastic-based ultrasonic stress measurement techniques is that the changes in wave velocity due to stress are very small, on the order of 0.0001% to 0.001% per MPa of stress [3, 18]. Very precise measurements are thus required, and stress-induced changes can easily be masked by other factors such as random or coherent noise, material composition, surface texture, grain microstructure, temperature, residual stress, and geometry variations due to in-field wear and tear. Because of these effects, while absolute stress measurements are possible in theory, a calibration measurement at a known stress is required in practice [18].

Nonlinear Guided Wave Propagation

Another type of ultrasonic testing which has shown promise is the so-called "nonlinear guided wave propagation" proposed by Nucera and Lanza di Scalea [34]. While the acoustoelastic effect is also a type of nonlinear guided wave propagation, this method leverages a different nonlinearity caused by potential energy storage due to "prevented thermal expansion", which results in the generation of a second-harmonic one octave higher than the excitation frequency. Since the appearance of the harmonic is stress dependent, the stress can be characterized by measuring a nonlinear parameter which quantifies the strength of the harmonic relative to the fundamental frequency. If measurements are made as the rail passes through the neutral temperature, this nonlinear parameter will appear to reach a minimum value, exposing the neutral temperature.

The authors present both lab and field testing, in which the neutral temperature can clearly be seen as a minimum in a plot of the nonlinear parameter versus time. Presumably, the limitation that the rail must pass through the neutral temperature during the test is what has held this measurement system from being widely adopted.

Rayleigh Wave Polarization

A third type of ultrasonic wave propagation testing is the Rayleigh wave polarization technique developed by Gokhale and Hurlebaus [16]. Since wave speed changes due to stress in the acoustoelastic effect are so small, the authors propose another mechanism for measuring stress, namely the polarization of Rayleigh waves, where polarization refers to the ratio of in-plane to out-of-plane deflection due to the propagating wave. The authors cite the nondispersive nature of Rayleigh waves, as well as the order-of-magnitude higher sensitivity of polarization to the stress compared with acoustoelastic wave velocities, as the

primary benefits of Rayleigh waves. Furthermore, the technique uses two laser vibrometers to measure the in-plane and out-of-plane motion, which enables a non-contact measurement. In practice, it was found that surface texture and conditions have a significant impact on measurements, likely requiring calibration at a known stress value.

Verse®

The only widely used and accepted non-destructive stress measurement technique is Verse®. Verse® is based on the simple principle that the transverse deflection of a stressed beam is related to the stress. The method works well and has been a commercially available solution for years; the only limitation is that the measurement process requires unfastening the rail for a considerable length on either side of the measurement location. Because of this, it does not satisfy the FRA's requirements for a NDE stress measurement technique.

Low-frequency vibration

At ultrasonic ranges, the stress dependence of wave velocities only appears in nonlinear elastic theories such as the acoustoelastic theory. At lower frequencies (below 1 kHz), however, assuming a linear elastic response is sufficient to introduce stress dependence into the model, and elementary theories such as Euler-Bernoulli or Timoshenko beam theory may be used[2]. Researchers have demonstrated the shift in natural frequencies of rails due to stress at these low frequency ranges, for example in [7, 30]. Standard modal analysis, however, is highly dependent on not just the material and geometry of the structure, but also the boundary conditions. In the field, the boundary conditions of the rail are highly variable, making standard modal analysis infeasible for measuring stress.

[2]While the stress dependence appears as a nonlinear geometric term (see Appendix A.1), the term can be linearized for small amplitude vibrations so that the governing equations are linear.

To overcome this, Damljanović and Weaver [11] proposed to fit a general modal solution consisting of several forward and backward propagating and evanescent modes to the forced vibration response of the rail at a resonant frequency. The authors use a surrogate finite element model to generate the expected wavenumbers in the general modal solution prior to applying boundary conditions, and then to perform a least-squares regression in order to 'fit' the terms related to boundary conditions. In the process, the authors also perform a secondary regression for a variation in the flexural wavenumber, in order to 'measure' the deviation from the expected wavenumber for zero stress. This deviation is subsequently correlated with the stress.

The work in this thesis is based on the same underlying principle as in Damljanović and Weaver [11], which is that the spectrum relation for a beam is independent of boundary conditions and encodes the stress contained in the structure. However, the details of the measurement and the subsequent data processing differ significantly in each technique.

Low-frequency flexural wave propagation

With a similar motivation to Damljanović and Weaver [11], namely to leverage the high stress sensitivity of low-frequency flexural vibrations while maintaining boundary-condition indifference, Albakri et al. [3] proposed using low-frequency flexural wave propagation for reference-free stress measurement. Unlike the steady-state response used in Damljanović and Weaver [11], Albakri's proposal was to use the same pulse-style excitation used in ultrasonic testing, but with very low carrier wave frequency. It was hypothesized that an appropriate actuator that could excite primarily a bending moment would isolate the flexural mode of interest from other contaminant modes. It was further hypothesized that a continuously welded (approximately 'infinite') rail would not contain significant reflection sources, especially since low frequencies tend to be more difficult to attenuate than higher frequencies.

Thus, wave propagation in principle should be independent of boundary conditions, unlike a steady-state based approach where reflections from the boundaries are allowed to saturate to form standing waves.

The technique that Albakri et al. [3] developed consisted of an optimization algorithm to fit a stress-dependent model to wave propagation measurements in order to estimate the stress. Using a first measurement of the isolated flexural mode, the algorithm would use the model to predict what a second measurement along the propagation path should look like. Minimizing the difference between the prediction and the actual second measurement served as a means to calculate the stress. The major challenge in this work, compared to existing ultrasonic wave propagation techniques, was accounting for strong dispersion. In non-dispersive or weakly dispersive wave propagation, the wave speed is independent or nearly independent of frequency; for example, acoustic waves in air travel at the same speed, regardless of frequency. Dispersive waves, on the other hand, have frequency-dependent wave speed; as a result, different frequency components travel at different speeds, and the wave 'disperses', or spreads out in space and time, as it propagates. Unlike the ultrasonic techniques which often use time-of-flight based measurements, the technique presented in [3] uses a truly dispersive, frequency-dependent formulation for the wave speed.

Experimental validation of the dispersive wave propagation technique was provided on a rectangular aluminum beam. The technique required significant manual signal processing to isolate the propagating wave from reflections, which limited the viable frequency range; however, the results confirmed that the technique was feasible. The main limitations that needed to be addressed in order to adapt the technique to in-field implementation included 1) developing compensation for reflections in order to eliminate any manual signal processing, and 2) making the technique more robust to random noise present in the field. The work presented herein is built upon the work of Albakri et al. and is aimed at addressing these

limitations.

1.2.2 Signal processing for noise compensation

Since the work in this thesis was aimed at bringing the work of Albakri et al. [3] closer to in-field implementation, the challenge of dealing with noise was identified as a major area of interest. The literature classifies noise into two categories: random noise and coherent noise [23]. Coherent noise generally refers to various unwanted wave modes in the structure, which can arise from a variety of sources including external excitation, material dispersion, and reflections from structural discontinuities. As a result, coherent noise tends to be the more significant challenge in the literature.

Random noise compensation: correlation techniques and time-diversity

Unlike steady state vibration, during which the structure is allowed to resonate and achieve high amplitude oscillations which can easily break the noise floor, wave propagation tests are inherently limited to small amplitude measurements. Even with optimal actuator and sensor selections, measurements can have difficulty breaking the noise floor. Various sources can give rise to random noise, including background noise (weather, outside traffic) and thermal noise in the material [6]. Nonetheless, since the noise is qualitatively distinct from the desired measurements in that it is random,several techniques can be effectively employed to reduce or eliminate random noise.

One class of commonly used techniques is correlation methods, in which a template signal is compared to the measurement in order to suppress particular regions and retain other regions in the measurement. A variety of such approaches exist, typically differentiated by the dictionary of template signals used to correlate with the measurement. Examples template

signals include using the known excitation pulse in non-dispersive measurements [28], using the known excitation with a dispersion compensation routine for dispersive measurements [27], and using wavelets for a combined time-frequency approach [22, 28].

Correlation based techniques essentially produce a new signal highlighting areas of high or low correlation with the template signal, effectively differentiating parts of the measurement which contain the desired signal and parts which contain unwanted random noise. While they are effective in damage localization settings, correlation methods are not suitable for the present work where the signal would need to be analyzed for stress measurement purposes. This is because they do not *remove* the random noise from the original signal; rather, they just specify portions of the signal which do or do not correlate with a particular template signal.

Another widely used technique for dealing with random noise in measurements is the technique of time-averaging, or taking multiple measurements and averaging them together. This technique is used throughout science and engineering, though it had not been implemented by Albakri et al. [3]. The fundamental principle behind time-averaging is that if a measurement is repeatable, different measurements will contain the same coherent desired signal, whereas the random portions will vary between measurements. As a result, adding the measurements together amplifies the coherent portions to a greater extent than the random portions, effectively boosting the signal-to-noise ratio (SNR). It is a well-known result that the SNR of time-averaged measurements increases as the square root of the number of measurements taken. For example, taking four measurements doubles the SNR compared to a single measurement; however, to achieve another two-fold increase then requires 16 measurements, so one encounters diminishing returns.

Time-averaging can also be classified as a type of diversity scheme, adopting the terminology used in the radar and communications industry. Various types of diversity schemes exist,

though the underlying principle is simple: various measurements are made while varying, or diversifying, some property of the measurement in order to improve the reliability of a signal. For example, using several radars placed at various locations can give higher confidence if each radar sees the same target; this is known as spatial diversity. In the same sense, if a signal is present in measurements made at various times, the signal can be considered more reliable; time averaging can therefore be regarded as a time-diversity scheme.

Coherent noise compensation: frequency-diversity

Another type of diversity scheme often used in communications systems is that of frequency-diversity. In radar systems, unwanted targets such as animals, the ground, or the ocean may be unintentionally detected, a phenomenon known as 'clutter'. Often, such clutter only occurs at particular frequencies; thus, by shifting the frequency of a radar system, one can distinguish desired targets as those which appear in every measurement, and undesired 'clutter' as targets which only appear at particular frequencies. Bilgutay [6] identified that material dispersion and grain noise in ultrasonic testing behave similarly to clutter in radar applications, in that the resulting coherent noise varies significantly with the excitation frequency. Rather than using measurements at different frequencies, the technique developed by Bilgutay [6], known as Split-Spectrum Processing (SSP), decomposes a signal into various component signals using bandpass filters to achieve frequency-diversity. Features which are present in every band are retained, whereas features only present in particular sub-bands are rejected.

While SSP is effective in certain applications, such as eliminating grain noise [6] and reducing dispersive modes [37] in ultrasonic testing, the method is also very sensitive to parameters such as the number, shape, and spacing of the bandpass filters [23] and the recombination algorithms used to reassemble the filtered signal [37]. In particular due to the inconsistent

nature of the recombination process used in SSP, the filtered signal is only qualitatively similar to the original signal. Again, for the purposes of identifying time-of-arrival of reflections for damage localization, such signal alteration is acceptable; however, a technique which alters the shape of the signal in such a manner is not suitable for the work in this thesis, where the filtered signal would have to be processed in order to extract wave propagation properties. The recombination technique would simply impose too much artificial content into the data, masking the features which are desired in this work.

In this thesis, the concept of frequency-diversity is employed in the traditional sense, in which measurements at various frequencies are made independently. The underlying motivation is always the same though: making measurements at many different frequencies decreases the impact of frequency-dependent measurement contaminants.

1.2.3 Dispersion curve measurement techniques

Through the process of deciphering the fundamental principle behind the low-frequency stress measurement technique in [3] in order to adapt it to cases with reflections, it was found that the method has more in common with dispersion curve measurement techniques than with other non-destructive stress measuring techniques commonly used in rails. The remainder of this section therefore focuses on techniques in the literature for explicitly measuring dispersion curves.

The most closely related dispersion curve measurement technique used in rails is that of ultrasonic wave propagation. As described in the Section 1.2.1 section, these techniques typically make single-frequency estimates of the phase velocity or group velocity dispersion curves using time-of-flight measurements and the simple relationship $v = \frac{\Delta x}{\Delta t}$. Besides the limitations described in Section 1.2.1, this technique gives a very low resolution measure-

ment of a dispersion curve, and is therefore only suitable for high frequency measurements where the dispersion curve remains relatively unchanged over a large frequency range. This technique is also severely limited regarding dispersion, random noise, and coherent noise in the form of reflections or mode conversion [40].

Another method used in the ultrasonic testing literature is that of using the Gabor wavelet transform (as demonstrated in [5]) or more generally what is referred to as 'time-frequency' analysis. In this approach, various types of transforms can be used to reveal the frequency content of a signal *as a function of time*. Doing so, one obtains peaks when a group of frequencies 'arrive' at a particular location at a specific time. This gives a slightly more rigorous way to determine a time-of-flight for a particular frequency in order to calculate the group velocity. Still, this method gives a very coarse dispersion curve and appears to be limited in regards to reflections or other forms of coherent noise. As such, it is not optimal for the low-frequency dispersion curves sought after in this work.

As an alternative dispersion-curve measuring technique, Albakri et al. [4] have also proposed a data-driven modeling technique based on steady-state measurements, for example from a standard modal test, rather than based on wave propagation measurements as in [3]. In this paper, the authors construct a data-driven model using rational approximation of the frequency response measurements from a modal test. The resulting state-space model is used to then simulate wave propagation measurements, and the same set of techniques from [3] are applied to the data. As a result, the results in [4] are still limited in their ability to handle low frequency cases with significant amounts of reflections or multiple wave modes. The work in this thesis can directly be applied to the results in [4] therefore to achieve a better estimate of the dispersion curve at low frequencies, which is a direct stated limitation in the cited paper.

It is worth mentioning that a large part of the guided wave literature is dedicated not to

measuring dispersion curves, but rather to *calculating* dispersion curves from various types of models. In fact, many papers relating to more accurate estimation of dispersion curves for rails exist, and many techniques such as finite element [5, 31, 42] and semi-analytical finite element [3, 26, 29, 36] methods have been applied to the problem. For the low frequencies in this work, Timoshenko beam theory has been shown to be sufficiently accurate [3], though if it is found in the future that a better model is necessary for the final curve-fitting step, this problem is well understood in the literature.

Looking outside of the guided wave literature, the geophysics and seismology communities also have relevant techniques to the measurement of dispersion curves. One commonly cited class of techniques produces an 'image' of a dispersion curve by applying a so-called *wavefield transformation* to the data; several transformations exist, two common ones being frequency-wavenumber and slowness-frequency transformations. In the work of Park et al. [35], frequency-dependent phase shifts or offsets are applied to a data set according to an assumed phase velocity, and the subsequent transformed wavefield contains local extrema where the assumed phase velocity correlates well with the data. When plotted as an image, this wavefield contains distinct streaks corresponding to the extrema which trace out the dispersion curves (see Park et al. [35] for examples of such figures).

This type of 'dispersion curve imaging' is useful when a relatively large number of traces, or measurements, are available (measurements at more locations give higher wavenumber resolution the same way that more samples in time give a higher frequency resolution). While the image is useful for potentially visualizing several wavemodes' dispersion curves at once, extracting the dispersion curves from the peaks can also present a challenge.

An elegant method to circumvent this and directly obtain the dispersion curves is presented in [39]. The authors first perform a Fourier transform along the spatial axis to convert measurements into the wavenumber domain; subsequently, they organize the data into two

snapshot Hankel matrices $\mathbf{X_1}$ and $\mathbf{X_2}$, shifted by one time-step. The authors then form the following matrix pencil: $\mathbf{X_2} - z\mathbf{X_1}$, where z has the form $z = e^{i\omega t}$. This matrix pencil, which resembles a wave-propagation solution, can then be solved as a generalized eigenvalue problem for the frequencies corresponding to the wavenumbers from the original transform. Alternatively, one can also perform a Fourier transform into the frequency domain and can solve the matrix pencil for the corresponding wavenumbers. Schopfer et al. [39] present very nice experimental validation of the technique at ultrasonic frequencies using a laser vibrometer and 488 scan points.

It is unclear how well this technique would apply to the cases considered in this thesis, where significantly fewer spatial measurements are used at a much lower frequency. One limitation, however, is that the technique does not appear to solve for the amplitude spectra of the various propagating waves. This information is useful for visualizing the various wavemodes as they propagate and verifying if the waves are being decomposed correctly.

1.3 Summary of results and organization of the thesis

In this thesis, a new signal processing technique for decomposing a signal into its forward and backward propagating components — for example to compensate for dispersive reflections — is presented. Additionally, the algorithm can be used to solve for the wavenumber, which is related to the propagation velocity, for each of these components. The collection of wavenumber estimates at various frequencies gives an estimate for the spectrum relation, or dispersion curve, for a structure, which can be used to fit an analytical model to the data in order to perform parameter estimation. This technique is used to successfully perform non-destructive stress measurement in the presence of dispersive reflections, and it can also simultaneously perform model updating to account for uncertainties in material and geom-

etry parameters. The performance is demonstrated on simulated and experimental data for a rectangular aluminum beam experiencing uniaxial stress.

The rest of the thesis is organized as follows. Chapter 2 begins with the theoretical formulation of the method, which is based on spectral analysis of wave propagation using the Fast Fourier Transform (FFT). An important graphical interpretation of the Fourier coefficients is presented, wherein the various frequency components are represented as vectors in the complex plane. This intuition is used as the basis for an algorithm for decomposing a wave into its forward and backward propagating components, as detailed in Chapter 3. The full general form of the problem is presented, along with some simplifying assumptions which are used to reduce the number of measurements needed.

Next, the algorithm is demonstrated on both simulated and experimental data in Chapter 4. The theory used to generate the simulated data is presented, and subsequently the ability of the algorithm to decompose the incident and reflected waves is shown. The performance of the algorithm regarding stress measurement is then demonstrated, first in a case where the material and geometry are taken as knowns, and subsequently in a case where some uncertainty is introduced regarding the material and geometry parameters. In both cases, the algorithm is successfully able to determine the stress.

The experimental setup used to validate the theory is described, and then the results of the algorithm are presented using both laser vibrometer measurements and accelerometer measurements. In the latter case, the model updating feature of the algorithm is demonstrated in its ability to account for uncertainty arising from mass-loading by the accelerometers.

The thesis is concluded in Chapter 5, where the future work is presented, followed by the bibliography and a collection of supplementary information in the appendix.

Chapter 2

Theory

Wave-propagation based stress measurement techniques seek to correlate changes in the propagation velocity of particular wave modes with changes in stress. At ultrasonic frequencies, stress measurement techniques such as in [8, 13, 16] typically employ a result from nonlinear theory of elasticity known as the acoustoelastic effect in order to obtain a measurable stress-dependent structural response. These techniques are inherently challenging to implement because the changes in wave velocities that must be measured are very small, on the order of 0.0001% to 0.001% per MPa of stress [18]. This relatively low sensitivity to stress can cause stress changes to be obscured by uncertainties in material and geometry properties Ultrasonic techniques based on the acoustoelastic effect therefore require precise characterization of the material and geometry properties of the waveguide, which in practice requires a reference measurement either at a known stress or on an identical separate test specimen [18].

The work herein is based on a different approach; while ultrasonic wave propagation techniques are often based on nonlinear elasticity, this work exploits a more prominent stress dependence found in the first order linear terms. The effect is most prominent in low-frequency flexural waves, so even approximate theories such as the Euler-Bernoulli or Timoshenko beam theories can be used with high accuracy. Furthermore, the changes in wave velocity due to stress for these low-frequency modes are much higher than the ultrasonic modes, on the order of 0.01% per MPa of stress, which eliminates the need for a reference

measurement. However, these low-frequency waves present two major challenges. First, they are significantly more dispersive than ultrasonic waves, which makes identifying the desired waves in measurements and processing them much more difficult. Second, the wavelengths for these low frequencies are much longer than those of ultrasonic waves; as a result, there is little or no separation between an original wave and subsequent reflections from waveguide discontinuities. Combined with their dispersive nature, these reflections can further complicate identifying the low-frequency waves of interest in measurements. These challenges are primarily what have deterred researchers from using low-frequency flexural waves in the past, despite their high sensitivity to stress.

2.1 Spectral analysis of wave propagation

The theory presented herein is based on spectral analysis of vibrations using the Fourier transform, as described in Doyle [12]. Since we are interested in dealing with discrete data from experiments, the formulation described in this thesis will use the discrete Fourier transform computed using the Fast Fourier Transform (FFT) algorithm[1]. According to the discrete Fourier transform (DFT), we can represent an arbitrary discrete time signal $F(t)$ as a superposition of sinusoidal signals[2]:

$$F(t) = \sum_{n=0}^{N-1} \hat{C}_n e^{i\omega_n t}, \tag{2.1}$$

[1]For details about the discrete vs. continuous Fourier transforms (DFT vs. CFT), sampling considerations, algorithmic implementation of the Fourier transform, and other important considerations, Doyle [12] provides a wonderful and thorough review of the topic with helpful graphics and examples.

[2]Note that we use a complex exponential representation for the sinusoidal terms, which relates to sine and cosine according to Euler's formula:

$$e^{i\omega_n t} = \cos(\omega_n t) + i \sin(\omega_n t)$$

where $\omega_n = \frac{2\pi n}{T}$ is the frequency of the n^{th} component in radians per second and N and T are the number of samples and the length of time of the sample, respectively. Here, $\hat{C}_n \in \mathbb{C}$ represents the Fourier coefficient for the frequency ω_n; the FFT algorithm returns a vector containing all of the Fourier coefficients.

There are a few important characteristics to note about the Fourier coefficients obtained using the FFT:

1. The first Fourier coefficient corresponds to $\omega_n|_{n=0} = 0$; this represents the DC offset, and as such it must be purely real.
2. The $(\frac{N}{2} + 1)^{th}$ coefficient, known as the Nyquist value, is also purely real.
3. Excluding the first coefficient, the remaining coefficients must be complex-conjugate symmetric about the Nyquist value.

These constraints are simply necessary in order to ensure that the complex components of the sum given in Eq. (2.1) cancel each other out in order to give a purely real time signal, and this can easily be verified using Euler's formula and carrying out the algebra; the only caveat is that the frequencies wrap around at the Nyquist value into the negative portion of the frequency axis.

Additionally, two important considerations about discrete time sampling are noted here:

1. While the continuous Fourier transform uses an infinite sum and can capture infinitely high frequency content, the discrete Fourier transform can only discern information up to the Nyquist frequency.
2. While the continuous Fourier transform can be used to represent a signal with 'infinite' period, the discrete Fourier transform implicitly assumes that the signal is periodic, with period corresponding to the length of the measured signal.

The implication of the first point is relatively straight-forward; in order to accurately capture high-frequency signal content, the data must be sampled at an adequately high sampling frequency. Note how in Fig. 2.1 (reproduced from [12]), since both datasets are sampled at the same sampling frequency, they are equally accurate (or inaccurate). The only way to increase the accuracy is to increase the sampling frequency to more accurately capture the higher frequency content.

The second point, however, has very important implications which can sometimes be exploited to achieve better results. In particular, if we 'zero pad', i.e. add zeros to the measured time signal, we can increase the *resolution* in the frequency domain. Note how in the top signal depicted in Fig. 2.1, adding more zeros to the time signal results in a closer spacing of points in the frequency domain. Again though, while the frequency resolution is higher, it is not any more accurate, so a sufficiently high sampling frequency nonetheless needs to be selected.

Since the signals considered here are wave pulses which should return to zero, padding with zeros is an appropriate way to approximate the real response which is only partly captured by a finite measurement. Assuming we have a high enough sampling frequency such that the DFT is a good approximation to the CFT, zero padding can therefore improve performance in some settings.

With these considerations in mind, we can use the definition given in Eq. (2.1) to represent measured vibration signals — for example, on a beam — as

$$u(x,t) = \sum_n \hat{u}_n(x) e^{i\omega_n t}, \tag{2.2}$$

where we have simply made some notational changes: $u(x,t)$ represents the deflection u of a beam at location x and time t, and $\hat{u}_n(x)$ gives the Fourier coefficient for angular frequency

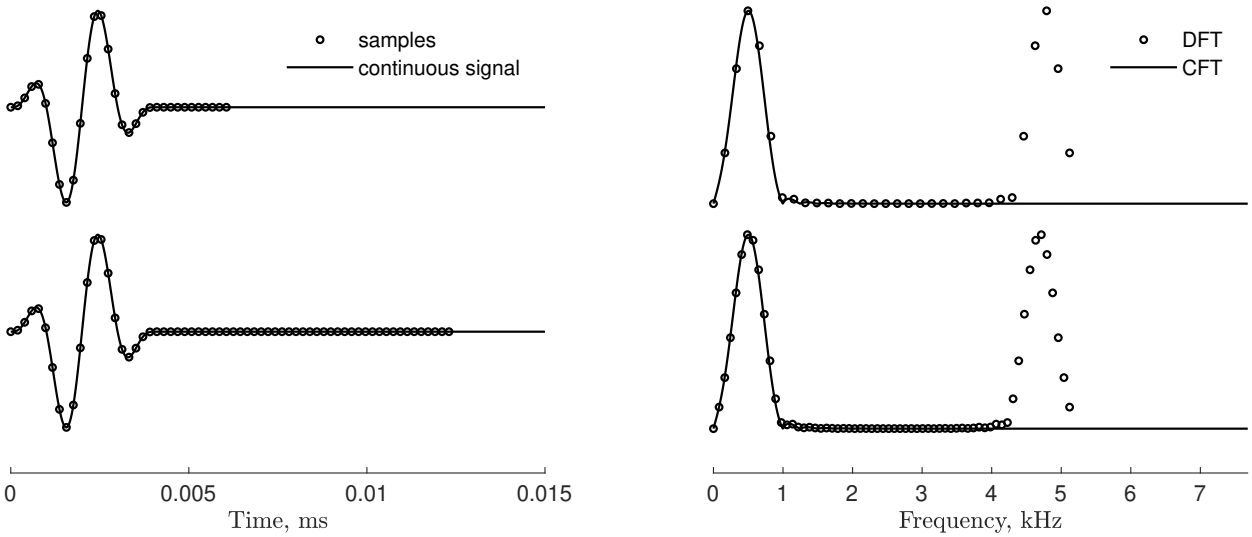

Figure 2.1: Effect of zero-padding on the frequency-domain representation. Note how for a fixed sampling frequency, padding with zeros to increase the number of samples (left) can increase the frequency resolution (right). The accuracy (or inaccuracy if the sampling frequency is not sufficiently high) is the same, but there are more samples along the curve of the continuous Fourier transform.

ω_n.

Using an accelerometer for example, we can measure $\ddot{u}(x,t)$, and passing this through the FFT algorithm gives $-\omega_n^2 \hat{u}_n(x)$. Since measuring acceleration, velocity, and displacement all give the same Fourier coefficients $\hat{u}_n(x)$ but just scaled by a constant factor of ω_n, in our analyses, we can treat them all as the main signal $u(x,t)$, as long as we are not mixing different measurement types together. Thus, from here on, rather than referring to acceleration, velocity, or displacement, they will all be referred to simply as *a measurement* $u(x,t)$.

Note that Eq. (2.2) decomposes the solution into a spatially dependent component (the Fourier coefficients $\hat{u}_n(x)$) and a time-dependent component; the Fourier transform essentially represents a separation of variables solution[3]. Going one step further, in wave-

[3]For more about this, see Appendix A.3.

propagation problems, the Fourier coefficients typically have the form

$$u(x,t) = \sum_n \hat{u}_n(x) e^{i\omega_n t} = \sum_n \hat{U}_n G(k_n x) e^{i\omega_n t},$$

where $\hat{U}_n$ is known as the *amplitude spectrum*, which is a property of the wave which is propagating, and $G(k_n x)$ is known as the *phase spectrum*, which represents a transfer function that determines how the wave appears at different locations on the waveguide. For the problems addressed in this thesis, the governing equations have constant coefficients, and the phase spectrum reduces to simply $G(k_n x) = e^{-ik_n x}$, where k_n is the spatial analog of angular frequency called the *wavenumber*. The so-called *spectral representation* of the solution to wave propagation problems can thus be given as

$$\begin{aligned} u(x,t) &= \sum_n \hat{U}_n e^{-ik_n x} e^{i\omega_n t} \\ &= \hat{U} e^{-i(kx-\omega t)}, \end{aligned} \tag{2.3}$$

where for notational simplicity, the summation and n subscripts are often understood but not explicitly written. What remains is to use the governing equations of the system to solve for the wavenumber k corresponding to each frequency ω. This 'spectral solution' is equivalent to a separation of variables solution; for an alternative derivation using traditional separation of variables notation, see Appendix A.1.1. The relationship between k and ω is called the spectrum relation, and it quantifies the relationship between periodicity in the spatial domain, characterized by k, and periodicity in the time domain, characterized by ω.

2.1.1 Graphical interpretation of wave propagation in the frequency domain

At this point, it is useful to interpret this spectral wave propagation solution in an intuitive manner in the frequency domain. Consider a time-domain vibration measurement of a wave propagation event, which can be represented in the form given in Eq. (2.3). The 'frequency-domain' representation of the signal is simply the Fourier coefficients of the signal, as obtained by performing a Fourier transform on the signal. As represented in the spectral solution in Eq. (2.3), the Fourier coefficients of an individual wave mode are given by $\hat{U}e^{-ik_n x}$, where $\hat{U}$ represents the amplitude spectrum and $e^{-ik_n x}$ represents the phase spectrum (which contains the spatial dependence of the solution). Recall, the phase spectrum can be thought of as a 'transfer function' which dictates how the wave (defined by the amplitude spectrum) manifests at different locations on the propagation path. It will be helpful to visualize this in the following manner: since the Fourier coefficients are complex numbers, each Fourier coefficient, i.e. the Fourier coefficient for a particular frequency, can be represented as a vector in the complex plane. The transfer function can then be interpreted as a rotation, since it is given by a circular function $e^{-ik_n x}$. 'Wave propagation' therefore corresponds to a rotation of the phase of the Fourier coefficients of the wave, while the amplitude of each Fourier coefficient is held constant[4].

Fig. 2.2 depicts the simple interpretation of wave propagation as a rotation applied to the Fourier coefficients of an incident wave. Note that the rotation *amount* is dependent on two values; the position x, and the wavenumber k_n. The spectrum relation can therefore be regarded as what determines how much each Fourier coefficient is rotated between different

[4]In the presence of damping, the frequency ω_n can be treated as a complex number such that the temporal solution has an exponential decay, though in this work it is possible to neglect dissipation. Similarly, if the wavenumber k_n is complex, there can be 'spatial damping' which is in fact a real, physical phenomenon known as evanescent waves; however, in this work it is appropriate to neglect this effect as well, as will be elaborated on further in the following section.

positions x along the waveguide.

2.2 Spectrum relation for Timoshenko beam theory

Continuing with the solution process, we must use the solution form given by Eq. (2.3) to solve the governing equations for the system of interest in order to obtain the spectrum relation; in other words, what remains is to solve for a spectrum relation which satisfies some governing equations. For the work presented in this thesis, a rail can be approximated at relatively low frequencies as an elementary beam. Here we use Timoshenko beam theory, which allows us to retain accuracy at higher frequencies than Euler-Bernoulli beam theory, but either could be used. Therefore, the derivation of the Timoshenko spectrum relation is presented here, whereas the Euler-Bernoulli spectrum relation derivation can be found in Appendix A.1 and follows the same procedure. We begin with the governing equations for a Timoshenko beam with axial load (see Appendix A.2 for the derivation of the governing equations).

TIMOSHENKO BEAM THEORY

$$\rho A\frac{\partial^2 u}{\partial t^2} - GA\kappa(\frac{\partial^2 u}{\partial x^2} - \frac{\partial \psi}{\partial x}) = 0 \tag{2.4}$$

$$\rho I\frac{\partial^2 \psi}{\partial t^2} - EI\frac{\partial^2 \psi}{\partial x^2} - GA\kappa(\frac{\partial u}{\partial x} - \psi) + F_0\frac{\partial u}{\partial x} = 0 \tag{2.5}$$

Here ρ is the material density, A is the cross-sectional area, $G = \frac{E}{2(1+\nu)}$ is the shear modulus, κ is the Timoshenko correction factor, I is the cross-section moment of inertia, E is the elastic modulus, and F_0 is the axial force. $u(x,t)$ is the beam deflection, whereas $\psi(x,t)$ is the rotation of the cross-section.

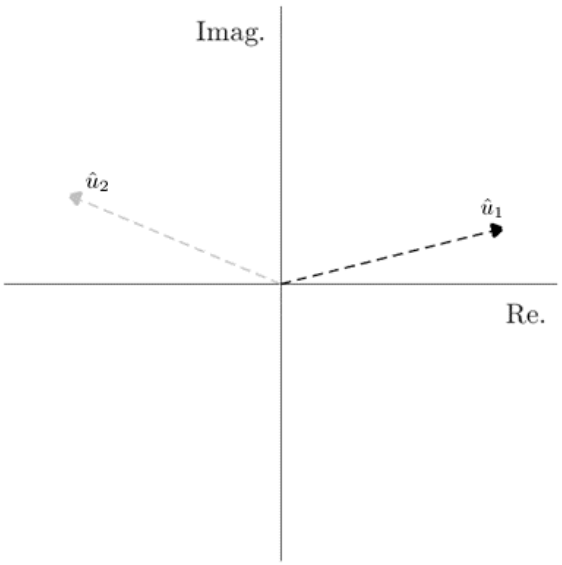

(a) Single mode measurements

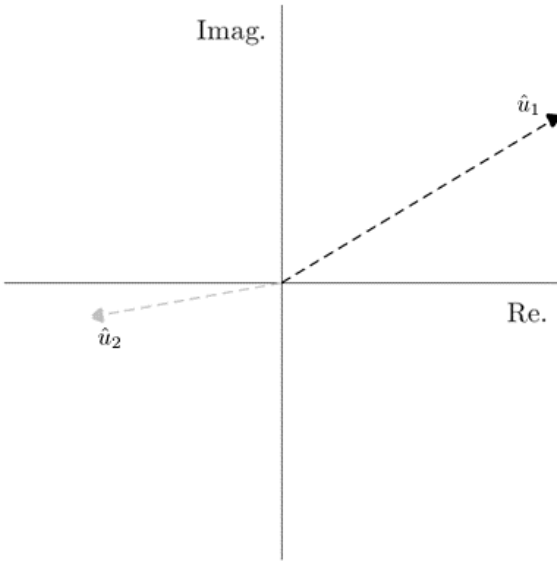

(b) Multi-mode measurements

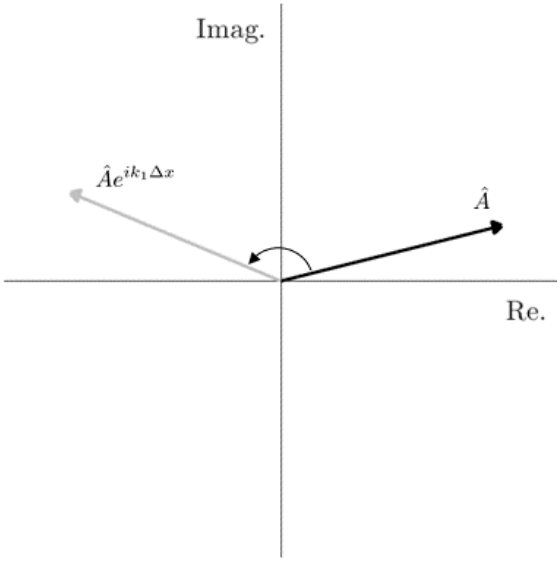

(c) Single mode identified

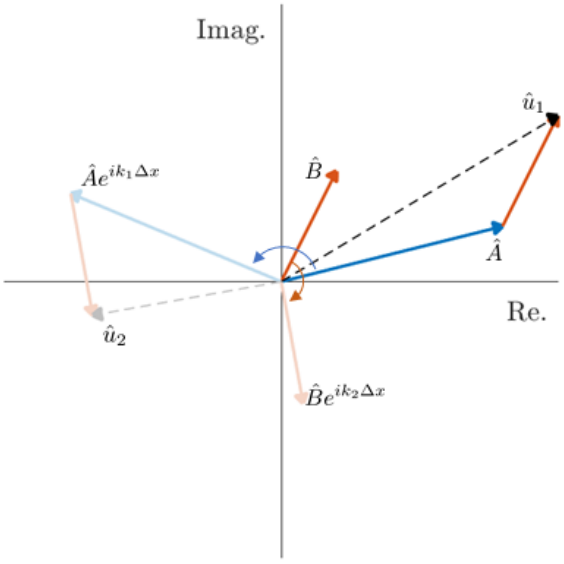

(d) Underlying multi-modes identified

Figure 2.2: Fourier coefficients plotted as vectors in the complex plane. 'Propagation' corresponds to rotating the phase of the vector while keeping the amplitude constant; for superimposed waves, this can be seemingly sporadic. Dotted lines represent raw measurements, whereas solid lines represent individual wavemodes, and in each case lighter lines of a same color represent a measurement at a distance Δx away from the first measurement. Note how in the case of a single mode, the measurement directly gives the modes, whereas for multi-mode cases (such as reflections), the individual unknown modes rotate and add up to the known measurements at each location.

We seek a spectral solution of the form

$$\mathbf{u}(x,t) = \widehat{\mathbf{U}} e^{-i(kx-\omega t)},$$

where $\mathbf{u}(x,t) = \begin{bmatrix} u \\ \psi \end{bmatrix}$ and $\hat{\mathbf{U}}(x) = \begin{bmatrix} \hat{U} \\ \hat{\Psi} \end{bmatrix}$. Derivatives with respect to space and time give the following:

$$\begin{gathered} \mathbf{u}(x,t) = \widehat{\mathbf{U}} e^{-i(kx-\omega t)} \\ \dot{\mathbf{u}}(x,t) = i\omega \widehat{\mathbf{U}} e^{-i(kx-\omega t)} \qquad \mathbf{u}'(x,t) = -ik\widehat{\mathbf{U}} e^{-i(kx-\omega t)} \\ \ddot{\mathbf{u}}(x,t) = -\omega^2 \widehat{\mathbf{U}} e^{-i(kx-\omega t)} \quad \mathbf{u}''(x,t) = -k^2 \widehat{\mathbf{U}} e^{-i(kx-\omega t)}. \end{gathered}$$

Thus, plugging the spectral solution into the governing equations transforms the differential equations into algebraic equations by means of eliminating the derivatives:

$$\begin{aligned} -\omega^2 \rho A \hat{U} \cancel{e^{-i(kx-\omega t)}} - GA\kappa(-k^2\hat{U} + ik\hat{\Psi}) \cancel{e^{-i(kx-\omega t)}} &= 0 \\ -\omega^2 \rho I \hat{\Psi} \cancel{e^{-i(kx-\omega t)}} + EIk^2 \hat{\Psi} \cancel{e^{-i(kx-\omega t)}} - GA\kappa(-ik\hat{U} - \hat{\Psi}) \cancel{e^{-i(kx-\omega t)}} - F_0 ik\hat{U} \cancel{e^{-i(kx-\omega t)}} &= 0. \end{aligned}$$

After cancelling all of the common exponential terms, the equations can be represented in matrix form as

$$\begin{bmatrix} -\rho A\omega^2 + GA\kappa k^2 & -iGA\kappa k \\ iGA\kappa k - iF_0 k & -\rho I\omega^2 + EIk^2 + GA\kappa \end{bmatrix} \begin{pmatrix} \hat{U} \\ \hat{\Psi} \end{pmatrix} = \begin{pmatrix} 0 \\ 0 \end{pmatrix},$$

for which a non-trivial solution requires the determinant of the coefficient matrix to be zero. The determinant of the coefficient matrix gives a quadratic polynomial for k^2:

$$AEGI\kappa k^4 + AF_0 G\kappa k^2 - \rho\omega^2 AEIk^2 - \rho\omega^2 AGI\kappa k^2 + \rho^2\omega^4 AI - \rho\omega^2 A^2 G\kappa = 0,$$

which can be simplified to the form

$$\underbrace{EI}_{a} k^4 + \underbrace{(F_0 - \rho\omega^2 \frac{EI}{G\kappa} - \rho\omega^2 I)}_{b} k^2 + \underbrace{\rho^2\omega^4 \frac{I}{G\kappa} - \rho A\omega^2}_{c} = 0.$$

The roots of this characteristic equation can be found using the quadratic equation with the coefficients a, b, c to give the two types of solutions for the wavenumber k as a function of frequency ω:

$$k_1 = \pm\sqrt{\frac{-b + \sqrt{b^2 - 4ac}}{2a}} \tag{2.6}$$

$$k_2 = \mp\sqrt{\frac{-b - \sqrt{b^2 - 4ac}}{2a}} \tag{2.7}$$

with $a = EI$, $b = F_0 - \rho\omega^2 \frac{EI}{G\kappa} - \rho\omega^2 I$, and $c = \rho^2\omega^4 \frac{I}{G\kappa} - \rho A\omega^2$.

These two solutions are called the *Timoshenko beam theory spectrum relations*, the plots of which are called dispersion curves and are shown in Fig. 2.3. k_1 is purely real valued and represents the propagating flexural wave mode (positive for forward propagating and negative for backward propagating). k_2 instead is purely imaginary at low frequencies and corresponds to an evanescent mode (now negative for forward propagating and positive for backward propagating). Despite having a somewhat non-intuitive 'imaginary' wavenumber/wavelength, evanescent modes *are* real, physical, and necessary to satisfy boundary conditions. Physically, evanescent waves correspond to spatially damped vibrations. Mathematically, this is evident because the imaginary wavenumber results in a real valued exponential decay spatial solution, which when paired with the oscillatory time solution gives these 'spatially damped' vibrations. To be clear, there is no damping, i.e. friction or dissipation, in this model;

evanescent modes are a purely geometric effect and are necessary for satisfying boundary conditions. In most cases, evanescent modes decay quickly, so they can often be ignored and indeed are ignored in the results of this thesis; however, the curious reader is encouraged to read further in Doyle [12] if interested. Another noteworthy feature of the evanescent modes in Timoshenko beam theory which can be seen in Fig. 2.3 is the transition above a cutoff frequency to a second (real valued) propagating mode (this does not occur in Euler-Bernoulli beam theory). However, this only happens at frequencies much higher than those considered in this thesis, so this effect is also ignored.

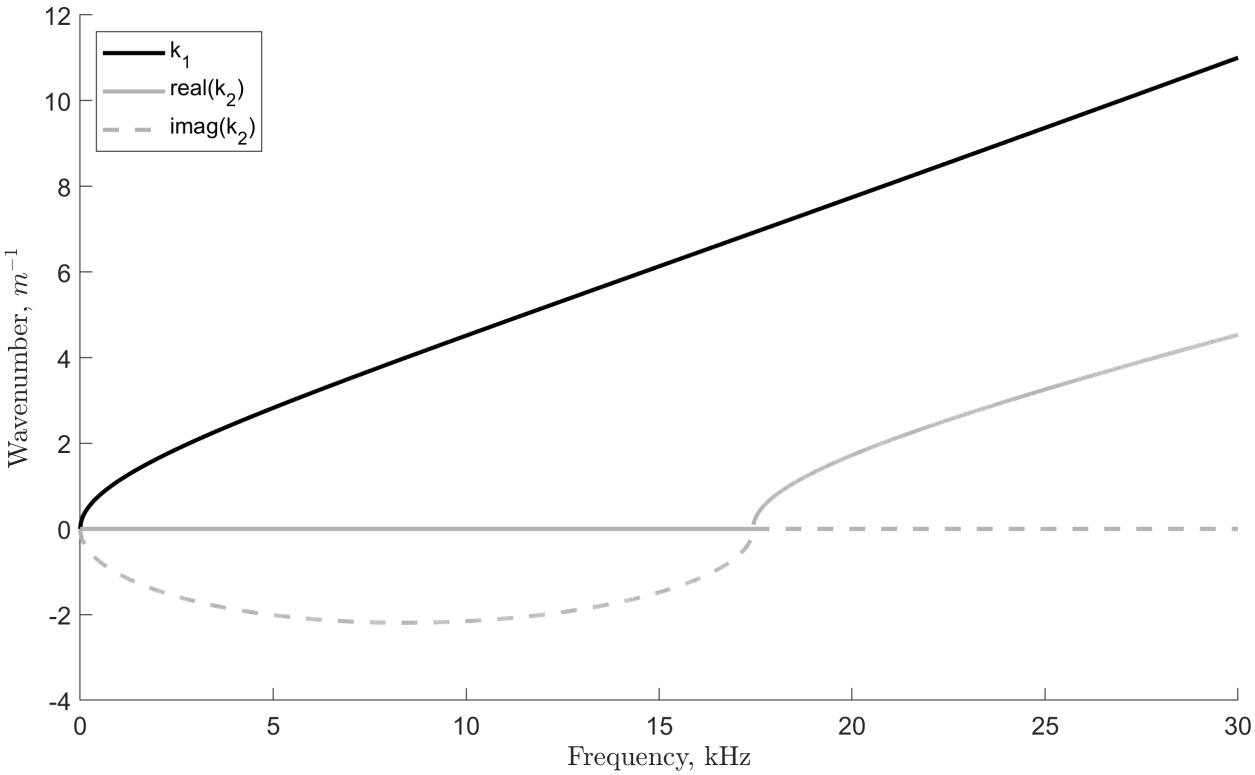

Figure 2.3: Timoshenko beam spectrum relations. k_1 is purely real for all frequencies and represents a propagating mode, whereas k_2 is only real and propagating above a cutoff frequency. Below that cutoff frequency, the imaginary wavenumber makes k_2 an evanescent, or spatially damped, mode.

2.2.1 Dependencies of the spectrum relation

Note how the spectrum relation Eq. (2.6) depends on the material, geometry, and stress parameters. Fig. 2.4 shows how the various model parameters affect the shape of the k_1 dispersion curve; in particular, note how stress uniquely determines the shape of the low-frequency portion of the curve. Therefore if we can measure the spectrum relation, it is possible to extract model parameters (or at least the lumped together a, b, and c constants) from the measured spectrum relation via a simple curve fit. Obviously we can solve for the stress this way, but it is also clearly possible to solve for other model parameters in the same manner, a feature known as 'model updating'. Model updating allows for handling uncertainty in the material and geometry parameters in the model, which in turn can help with increasing the accuracy of the stress measurement.

2.2.2 More on geometric dispersion

An important feature of flexural waves in beams is the dispersion effect. Consider momentarily the spectrum relation for axial or torsional waves in *rods* (or identically waves in strings)[5]: $k = \sqrt{\frac{\rho}{E}}\omega$. This spectrum relation is linear, and thus the phase velocity $c_p = \frac{\omega}{k} = \sqrt{\frac{E}{\rho}}$ is constant and does *not* depend on frequency. Since the phase velocity is the same for each frequency, every frequency component travels with the same velocity, and the wave pulse will therefore maintain its shape as it travels, as shown in Fig. 2.5a.

[5]This can be obtained using the same process as shown in Section 2.2 and Appendix A.1.1, but instead using the governing equations for a string or rod, i.e. the 1D wave equation:

$$\ddot{u} = c^2 u''$$

.

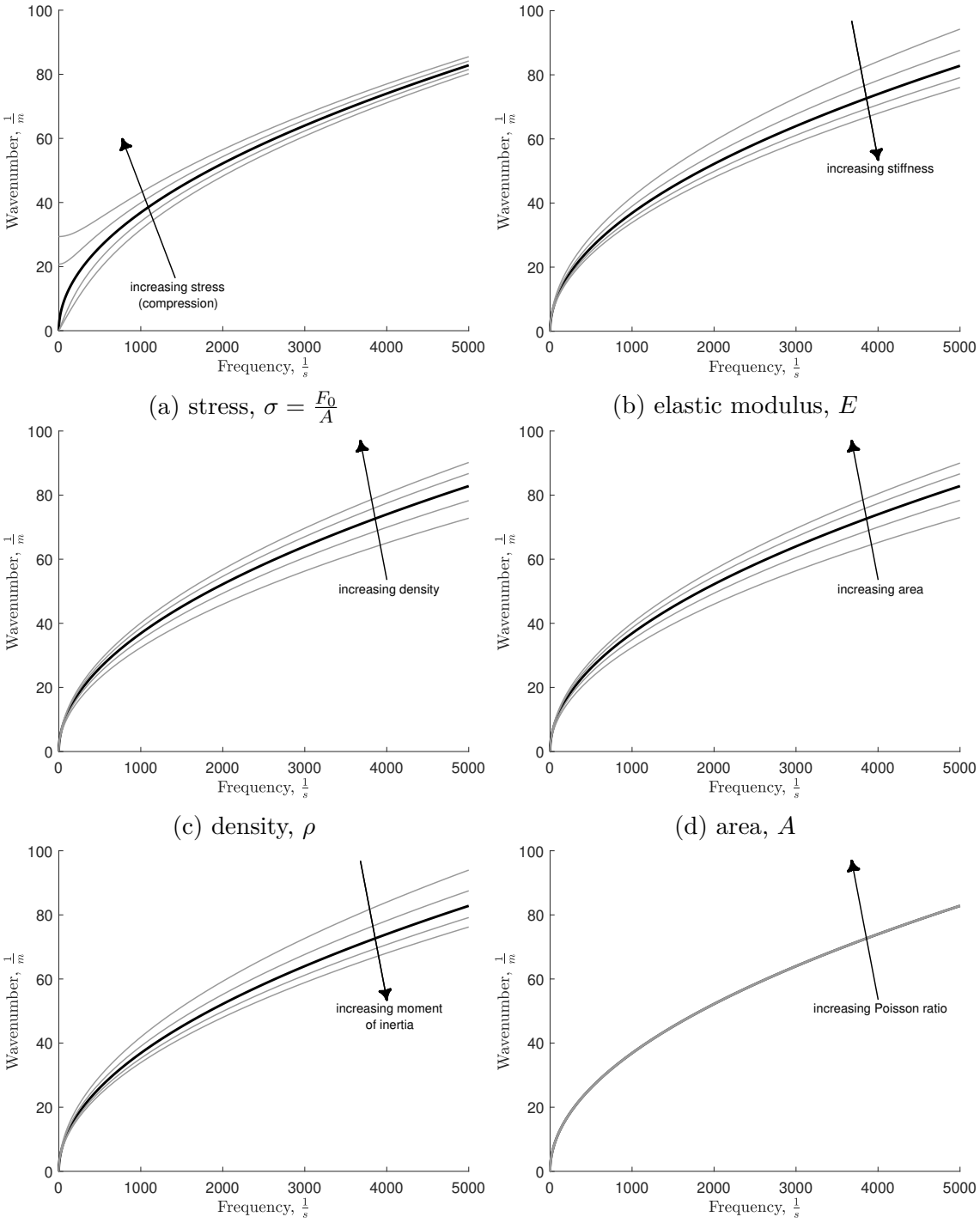

(a) stress, $\sigma = \frac{F_0}{A}$

(b) elastic modulus, E

(c) density, ρ

(d) area, A

(e) moment of inertia, I

(f) Poisson ratio, nu

Figure 2.4: The qualitative effects which various model parameters have on the spectrum relation. Note that the stress uniquely determines the low frequency portion of the curve, whereas all the model parameters affect the high frequency portion in a similar manner. The Poisson ratio seems to have little effect on the dispersion curve compared with the other parameters.

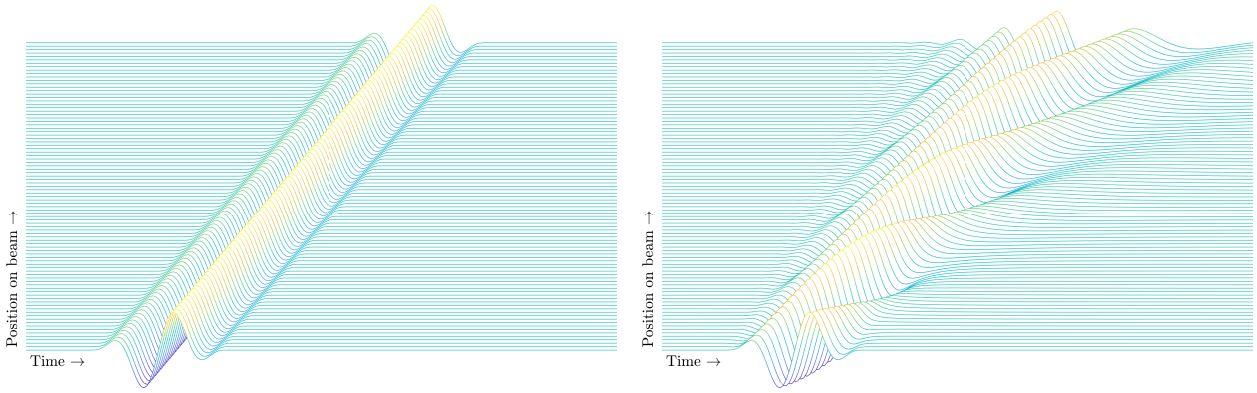

(a) A non-dispersive wave.

(b) A dispersive wave.

Figure 2.5: Comparison between dispersive and non-dispersive wave propagation. In both figures, the responses at various locations are stacked in order to show the vibration as it travels in space and time; lines correspond to individual measurements from separate locations.

Now instead consider the spectrum relation for waves in a beam, as derived[6] from either Euler-Bernoulli or Timoshenko beam theory:

$$k = \sqrt{\frac{-b + \sqrt{b^2 - 4ac}}{2a}},$$

$$\text{with} \begin{cases} \text{Euler-Bernoulli:} & a = EI,\ b = F_0,\ c = -\rho A\omega^2 \\ \text{Timoshenko:} & a = EI,\ b = F_0 - \rho\omega^2 \frac{EI}{G\kappa} - \rho\omega^2 I,\ c = \rho^2\omega^4 \frac{I}{G\kappa} - \rho A\omega^2 \end{cases}$$

The relationship between k and ω is no longer linear, as can most easily be seen in Fig. 2.3. As a result, the phase speed $c_p = \frac{\omega}{k}$ is not constant, but rather is frequency dependent, and each frequency component in a signal will travel at a different speed. Even in the absence of the axial load F_0, the flexural mode is still dispersive. **To be clear, this is**

[6] the derivations of both beam theories are provided in Appendix A.1 and A.2

not a nonlinear effect or to be confused with the acoustoelastic effect relating to nonlinear elasticity. This geometric dispersion[7] and the stress dependence of the spectrum relation follow from the derivation of Timoshenko beam theory, which assumes a linear elastic material response according to Hooke's law. While the axial loading is introduced as a geometrically nonlinear term, it is linearized for small displacements and the resulting governing equations are ultimately linear. Geometric dispersion has the effect of causing the wave pulse to 'spread out' and change shape as it travels (see Fig. 2.5b), making time-of-flight measurements ill-posed.

2.3 Reflections

The theory presented thus far, namely the spectral representation of wave motion and the spectrum relation which governs that wave motion, are sufficient to already model simple wave propagation problems and even analyze simple cases of experimental data. Recalling Eq. (2.3)

$$u(x,t) = \hat{U} e^{-i(kx-\omega t)},$$

for a given (input) amplitude spectrum $\hat{U}$, Eq. (2.3) specifies how the wave will appear for all points x and times t. Eq. (2.3) essentially 'propagates' the wave $\hat{U}$ to any location. In a simulation setting, $\hat{U}$ would be prescribed as the incident wave; however, in an experimental setting, a first measurement might be made in order to *measure* the incident wave $\hat{U}$. For a given set of material and geometry parameters, which define a spectrum relation k, Eq. (2.3) then essentially defines a model for the test article. Subsequent measurements can then be compared to the model, and the difference between the measurements and the model's

[7] as opposed to material dispersion

predictions can then be used as the basis for an optimization to match the model to the test article. This is essentially the procedure given in Albakri and Tarazaga [2], Albakri, Malladi, and Tarazaga [3].

In reality, we often do not see a single wave pulse traveling unobstructed off to infinity; real structures contain boundaries and other discontinuities which may impede the wave's ability to propagate, and we subsequently see waves reflected from these discontinuities. Thus, while boundary conditions do not affect a wave as it propagates, they can cause mode conversion (the most common being forward to backward conversion, i.e. a reflection).

While Eq. (2.3) can be used to represent a single wave mode propagating along a structure, it does not represent the structure's full possible response. Recall that the spectrum relation gave two types of solutions, the propagating flexural solution and the evanescent solution, and that each solution could either be positive or negative, corresponding to forward or backward propagating solutions. The total response for a single waveguide can therefore be a superposition[8] of these four individual solutions:

$$u(x,t) = (\hat{A}e^{-ik_1 x} + \hat{B}e^{-ik_2 x} + \hat{C}e^{ik_1 x} + \hat{D}e^{ik_2 x})e^{i\omega t}, \tag{2.8}$$

where $\hat{A}, \hat{B}, \hat{C}, \hat{D}$ are the amplitude spectra for the various solutions.

In order to model a waveguide with reflection sources, such as boundaries or discontinuities, we simply join various smaller waveguides and match the boundary conditions between them, solving for the amplitude spectra of the various wave modes $\hat{A}_i, \hat{B}_i, \hat{C}_i, \hat{D}_i$ for each waveguide. For example, we might prescribe only a forward propagating incident wave $\hat{A}_1$ in a simulation, but in order to satisfy the boundary conditions, a reflected mode $\hat{C}_1$ may turn out to be necessary. For a beam, four boundary conditions at each boundary are

[8] This is of course only possible because of the linearity of the governing equations.

required, corresponding to the displacement, slope, bending moment, and shear force. The mathematical descriptions of these quantities are provided in Table 2.1.

Table 2.1: Boundary conditions for a beam.

	Euler-Bernoulli	Timoshenko
Displacement:	$u = u(x,t)$	$u = u(x,t)$
Slope:	$\psi = \frac{\partial u}{\partial x}$	$\psi = \psi(x,t)$
Moment:	$M = EI\frac{\partial^2 u}{\partial x^2}$	$M = EI\frac{\partial \psi}{\partial x}$
Shear Force:	$V = -EI\frac{\partial^3 u}{\partial x^3}$	$V = -GA\kappa(\frac{\partial u}{\partial x} - \psi)$

For the purposes of the algorithm for analyzing wave propagation measurements for stress though, the measurement will simply see various wave modes and be agnostic as to their sources, so the boundary conditions are insignificant in regards to the forthcoming algorithm.

The inability to handle multiple modes or reflections is a major limitation in many existing wave propagation techniques [3, 40]. These techniques have difficulty with reflections because they are based in the time domain, whereas the various wave modes are only separable in the frequency domain. Consider the non-dispersive incident and reflected waves in Fig. 2.6a; one could feasibly 'cancel out' the reflection in the time domain by identifying the reflection at a location where it does not overlap with the incident wave, inverting it, and then 'shifting' the wave the appropriate amount in the rest of the data to negate the reflection. For the dispersive case such as in Fig. 2.6b, this intuition about inverting and shifting the wave in the time domain becomes much more complicated, because 'shifting' the wave corresponds to rotating the phase in the frequency domain, and for dispersive waves, the appropriate phase rotation is frequency dependent. Thus rather than performing the phase shift uniformly in the time domain, it must be performed independently for each frequency component in the frequency domain.

This problem is exacerbated by the fact that the global views in Figs. 2.6a and 2.6b are not

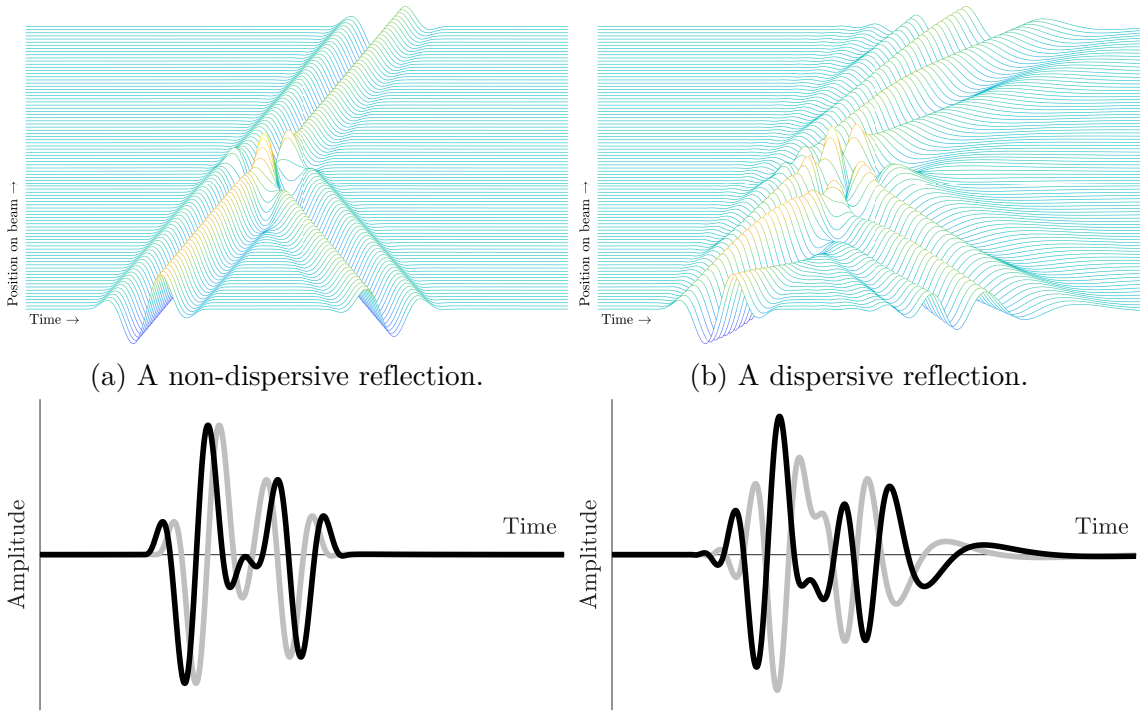

(a) A non-dispersive reflection.

(b) A dispersive reflection.

(c) Example measurement for a non-dispersive reflection.

(d) Example measurement for a dispersive reflection.

Figure 2.6: Comparison between dispersive and nondispersive reflections. In the bottom figures, the dark line corresponds to a sensor closer to the wave source, whereas the light line corresponds to a sensor closer to the reflection source.

often available, and instead we must infer the systems behavior from limited measurements such as those in Figs. 2.6c and 2.6d which may not clearly identify the incident or reflected wave. Furthermore, even if one could identify one of the waves, it is not guaranteed that all of the other wave modes propagate with the same dispersion relation.

In the frequency domain, since the descriptions for the various waves at all locations are simply linearly superimposed as in Eq. (2.8), it is possible to apply not only a frequency-dependent phase shift, but also a mode-dependent phase shift.

Consider the graphical interpretation of wave propagation presented in Section 2.1.1, wherein the wave propagation problem is represented as a rotation of the Fourier coefficient 'vectors'

in the complex plane. In the case where a single wave mode is present in the structure, the Fourier transform of a vibration measurement directly gives the wave's Fourier coefficients; therefore the graphical representation of each Fourier coefficient at different locations manifests simply as a vector rotating about the origin[9], as shown in Fig. 2.2c. When multiple wavemodes are present, the Fourier transform of a vibration measurement will no longer give the Fourier coefficients of a single wave mode; rather, it will give the *sum* of the Fourier coefficients of the various wavemodes. If the Fourier transform of the measurements is plotted as a vector in the complex plane as before, it will no longer simply rotate around the origin. Instead, it will appear to somewhat sporadically change lengths and direction, as depicted in Fig. 2.2b.

The problem of identifying dispersive reflections therefore can be interpreted in the frequency domain as the problem of identifying the vectors which, when rotated independently by the appropriate amounts and in the appropriate directions, add up to the full vector given by the measurement. This 'vector addition' problem forms the foundation of the algorithm presented next in Chapter 3.

[9]This simplified case corresponds to the algorithm presented Albakri et al. [3].

Chapter 3

Algorithmic implementation

In order to measure stress, we must solve the inverse problem of analyzing measurements and uncovering the model parameters which best match the data. Each measurement corresponds to an 'equation' which may be used to solve for an unknown; the number of measurements required depends on the number of model parameters which are unknown. However, adding more measurements and solving in a least-squares sense can increase the robustness of the technique to experimental uncertainty and random noise. Consider the general 'theoretical' form for a vibration signal measured from a wave propagation experiment on a beam, i.e the general solution from Eq. (2.8):

$$u(x,t) = (\underbrace{\hat{A}e^{-ik_1x}}_{\text{forward propagating}} + \underbrace{\hat{B}e^{-ik_2x}}_{\text{forward evanescent}} + \underbrace{\hat{C}e^{ik_1x}}_{\text{backward propagating}} + \underbrace{\hat{D}e^{ik_2x}}_{\text{backward evanescent}})e^{i\omega t}.$$

In general, the unknowns in this solution are $\hat{A}, \hat{B}, \hat{C}, \hat{D}, k_1,$ and k_2. These[1] correspond to all four wavemodes' Fourier coefficients and their two distinct spectrum relations (with of course appropriate signs for forward and backward propagating). In total, there are 6 complex unknowns, thus requiring 6 measurements in order to 'close' the system. The 6

[1]Note: these are all complex numbers, so in reality each variable corresponds to *two* unknowns; however, each measurement corresponds to a complex equation or two scalar equations in the frequency domain, so for simplicity we will treat each complex number as a single unknown unless stated otherwise.

measurements will each give an equation of the form

$$\hat{u}(x_i) = \hat{A}e^{-ik_1x_i} + \hat{B}e^{-ik_2x_i} + \hat{C}e^{ik_1x_i} + \hat{D}e^{ik_2x_i},$$

where $\hat{u}(x_i)$ is simply the Fourier transform of the time-history at position x_i. The collection of measurements $\hat{u}(x_i)$ form a nonlinear system of equations[2] which can be solved at every frequency for the problem's unknowns $\hat{A}, \hat{B}, \hat{C}, \hat{D}, k_1,$ and k_2. As described in Section 2.1.1 and Section 2.3, this nonlinear system of equations corresponds to a vector addition inverse problem in which a set of unknown vectors which rotate by unknown amounts are deduced from their sums.

Two simplifying assumptions which can be used to reduce the number of unknowns and potentially make solving this system easier include

1. Assuming the evanescent terms are negligible; since evanescent modes decay quickly in space, this is often a good assumption.

2. Assuming the evanescent wavenumber is $k_2 = -k_1$; for all but very high frequencies this holds true, and in Euler-Bernoulli beam theory this is the exact solution.

With assumption 1) in particular, the number of unknowns can be cut in half, only requiring 3 measurements (i.e. 3 sensors) to theoretically fully define the system. It should be noted here that the nonlinear system of equations is not guaranteed to have a unique solution. However, in practice this formulation has been found to converge much more reliably than the time-domain based optimization problem found in [3]. Furthermore, the system of equations

[2]This system of equations can be solved in rectangular coordinates, i.e. real and imaginary components, or alternatively in polar coordinates, i.e. amplitude and phase. Because of the non-uniqueness of polar coordinates due to the wrap around every 2π radians, we choose to solve the system in terms of the real and imaginary components. Solving in the time domain using the 2-norm of the error between the prediction and measurement, as in [3], implicitly forces one to solve in terms of amplitude and phase, introducing convergence issues due to the wrap around effect.

can be overdetermined with additional measurements, allowing us to solve the system in least-squares sense to aid with noise from experimental data.

Each measurement then takes the form

$$\hat{u}(x_i) = \hat{A}e^{-ik_1 x_i} + \hat{C}e^{ik_1 x_i}.$$

If the goal is to simply remove the reflected signal contamination or to obtain an estimate of the dispersion curve, one can stop here. In this work, this set of equations is solved using MATLAB's built-in `lsqnonlin()` function, which solves the system iteratively. The initial guess for each of the unknown amplitude spectra's first frequency bin is zero, and subsequent frequencies use the previous frequency's solution as an initial guess. The initial guess for the unknown wavenumber at each frequency is taken from the zero-stress dispersion curve for the nominal waveguide.

To restrict the solution space in order to further aid convergence speed and reliability, some relatively straightforward bounds are imposed on the unknown variables. The amplitude spectra components are given a lower bound of zero in order to avoid mixing up forward and backward propagating components. For the upper bound, the magnitude of the amplitude spectrum of the input is normalized to the largest component in the measurement; this just provides a conservative upper bound on the energy that is possible in the signal based on the known input. For the dispersion curve, a lower bound of zero is used. For the upper bound, the dispersion curve is modified so that it deviates 20% higher than nominal for the material/geometry parameters, whereas the stress is set to a high value above the theoretical buckling load of the beam. These bounds are not necessarily optimal, and performance could potentially be improved; however, in practice, the algorithm converges quickly and reliably to a reasonable solution in both simulated and experimental data.

After solving the nonlinear system of equations at every frequency, the solution will be the set of previously unknown system parameters $\hat{A}, \hat{B}, \hat{C}, \hat{D}, k_1,$ and k_2 (or a subset of these parameters if some are neglected).

However, to measure stress or other model parameters, one additional step is required. The model information, such as stress or the elastic modulus, is encoded in the spectrum relation $k_1(\omega)$ (or alternatively k_2 could be used). This 'cloud' of dispersion curve estimates can be fit with the analytical Timoshenko dispersion curve Eq. (2.6) as a means of system identification; in other words, we can use a least-squares fitting technique to find the model parameters[3] which best 'match' the cloud of dispersion curve estimates. Since the analytical spectrum relation is nonlinear for the dispersive waves in question, an iterative nonlinear least-squares solver must be used. In this work, MATLAB's built in `lsqnonlin()` function was used.

The wavenumber estimates are only expected to be accurate for frequencies with significant enough energy content. We can therefore use the magnitude[4] of the input wave's amplitude spectrum as a weighting; frequencies near the center frequency have high energy and can be trusted more, whereas frequencies far away with little energy will be more susceptible to noise and should be trusted less. To obtain an estimate of a larger range of the dispersion curve, we can then use wave pulses at various center frequencies to piece together different regions of the dispersion curve.

Pseudocode for the entire process[5] for measuring stress from a set of wave propagation

[3] See Fig. 2.4 to observe how the various model parameters affect the dispersion curve. Note how stress uniquely determines the low-frequency portion of the curve.

[4] or multiples of the magnitude; for example, the Power Spectral Density (PSD) is the magnitude of the amplitude spectrum squared.

[5] Note that the algorithm does not require any pre-processing of the data in the form of windowing the response or filtering the response; preliminary investigations suggest that windowing the response imposes undesirable artifacts into the results, and the frequency-dependent weighting according to the power spectral density of the input indirectly filters unwanted noise sufficiently.

Although not necessary, the program can be accelerated by only solving the nonlinear system of equations

measurements is provided in Algorithm 1, and the full MATLAB implementation can be found on github. Note that the dispersion curve estimates from each trial are appended to a list which collects all of the results; that is, every trials frequency vector ω, wavenumber vector k_1, and weighting vector are appended to the collective ωs, ks, and ws, respectively, so that the whole dispersion curve can be constructed from the individual pieces from each trial.

Algorithm 1: Stress-measurement algorithm in the presence of reflections

Data: $u^{(i)} \equiv$ Vibration measurements from various frequency pulses,
$x^{(i)} \equiv$ Sensor locations,
$F_{in} \equiv$ Forcing input signal.
Result: $\sigma \equiv$ Stress estimate
for *every frequency pulse trial* **do**
$\hat{u}^{(i)} = \texttt{fft}(u^{(i)})$ `// Perform FFT on the data`
Solve the nonlinear system of equations: `// for every frequency component`
$\hat{u}^{(1)} = \mathbf{A}e^{-ik_1x^{(1)}} + \mathbf{C}e^{ik_1x^{(1)}}$
$\vdots$ `// an equation corresponding to each sensor at location` $x^{(i)}$
$\hat{u}^{(i)} = \mathbf{A}e^{-ik_1x^{(i)}} + \mathbf{C}e^{ik_1x^{(i)}}$
Solution: $\rightarrow \underbrace{\mathbf{A}}_{\text{Forward-propagating wave}}, \underbrace{\mathbf{C}}_{\text{Backward-propagating wave}}, \underbrace{k_1}_{\text{Spectrum relation}}$
Store the dispersion curve estimates:
$\omega s = [\omega s;\ \omega]$ `// FFT frequency vector`
$ks = [ks;\ k_1]$ `// Spectrum relation`
$ws = [ws;\ abs(fft(F_{in}))]$ `// Weighting based on input energy`
end
Weighted nonlinear least-squares fit to find model parameters:
Fit data $\omega s, ks, ws$ using a model dispersion curve: $\underbrace{k = f(\omega; \sigma, E, I, \rho, A, ...)}_{\text{(e.g. Timoshenko spectrum relation)}}$
Solution: $\rightarrow \sigma,$ optionally $E, I, \rho, A,$ etc.

for Fourier coefficients above a particular threshold, i.e. ignoring Fourier coefficients or frequencies with negligible energy.

Chapter 4

Results

4.1 Simulation setup

In order to first validate the performance of Algorithm 1 on a controlled and noise-free dataset, the analytical Timoshenko beam solution is used to simulate a theoretical response on which to test the algorithm. The model consists of an infinite beam with a concentrated mass located at the center; this was chosen to simulate a discontinuity such as a weld joint in continuously welded rail. For this work, a 'worst-case' scenario was determined to be a reflection source with low admittance, such that a large portion of the incident wave is reflected and interferes with the slower portions of the incident wave. The mass m_j of the concentrated mass is therefore set arbitrarily high and placed at the center of the beam ($x = 0$), as illustrated in Fig. 4.1.

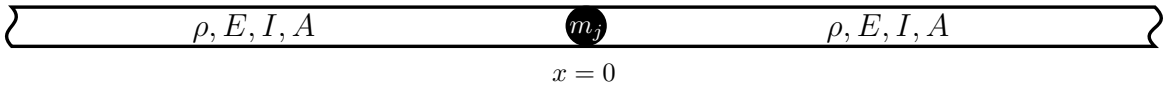

Figure 4.1: Simulated waveguide with a concentrated mass at the center acting as a reflection source.

The model parameters for the simulation are as follows:

Table 4.1: Model parameters used in the simulation.

	Geometry	
W	width	3.81 cm
T	thickness	3.175 mm
d	reflection distance	0.5 m
A	cross-section area	$W \cdot T$
I	cross-section moment of inertia	$\frac{1}{12} W \cdot T^3$
	Material	
ρ	density	2700 kg/m^3
E	elastic modulus	69 GPa
ν	Poisson ratio	0.33
α	thermal expansion coefficient	$22 \cdot 10^{-6}$ °C^{-1}
m_j	point mass	10^9 kg

Practically, we then model this as two separate beams which are joined together at the concentrated mass. Each beam satisfies the Timoshenko beam governing equations, and as such has a general response as described in Eq. (2.8) in Section 2.2:

$$u_i(x,t) = (\hat{A}_i e^{-ik_1 x} + \hat{B}_i e^{-ik_2 x} + \hat{C}_i e^{ik_1 x} + \hat{D}_i e^{ik_2 x}) e^{i\omega t}, \quad \text{for } i = 1, 2$$

$$\text{with } k_{1,2} = \sqrt{\frac{-b \pm \sqrt{b^2 - 4ac}}{2a}}, \quad \begin{cases} a = EI, \\ b = (F_0 - \rho\omega^2 \frac{EI}{G\kappa} - \rho\omega^2 I), \\ c = \rho^2\omega^4 \frac{I}{G\kappa} - \rho A \omega^2, \end{cases}$$

where k_1 corresponds to the plus and k_2 the minus in the numerator. The total response is simply the union of the two responses u_1 and u_2, where $u_1(x,t)$ is the response of the beam to the left of the joint, i.e. for $x \leq 0$, and $u_2(x,t)$ is the response of the beam to the right of

the joint, i.e. for $x \geq 0$.

We prescribe the incident wave as a two-cycle sine wave with center frequency Ω, amplitude modulated by Hanning window[1] to give the signal shown in Fig. 4.2.

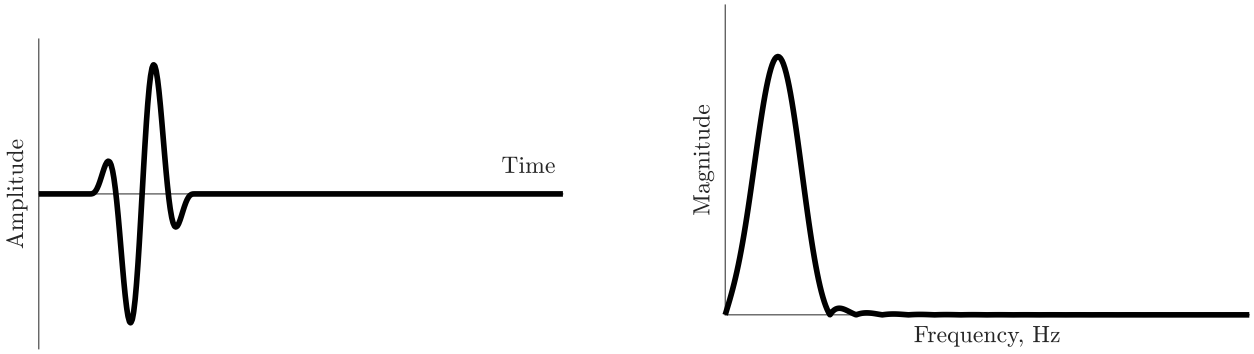

(a) Two-cycle Hanning toneburst.

(b) Amplitude spectrum of the two-cycle Hanning toneburst.

Figure 4.2: Time and frequency domain representations of the incident waveform.

The incident wave is prescribed in the simulation by simply setting the amplitude spectrum of the right-propagating component of the solution in the left beam to be the Fourier transform of the two-cycle toneburst, i.e. in MATLAB notation `A1 = fft(y)` $e^{ik_1 l}$, where `A1` is the amplitude spectrum of the right propagating component in the left half of the beam and `y` is the toneburst signal. The $e^{-ik_1 l}$ component, where l is some distance away from the center of the beam, is necessary to specify where the wave originates from, and is just a result of placing the origin at the mass rather than placing the mass a distance l from the origin. Since the evanescent term dies out quickly and is typically due to a boundary, we set $\hat{B}_1$ to zero. We can also use intuition to note that the beam after the joint will not have any leftward propagating components $\hat{C}_2$ and $\hat{D}_2$. However, $\hat{C}_1$ and $\hat{D}_1$, representing the reflected propagating and evanescent modes in the beam on the left side of the joint, must be determined by satisfying boundary conditions. Similarly, $\hat{A}_2$ and $\hat{B}_2$, representing the

[1] This particular incident waveform was determined to be optimal for this application in [3].

transmitted propagating and evanescent modes which continue to travel forward through the joint, must be solved for by satisfying boundary conditions. In all, there are 4 unknown amplitude spectra, which are determined by satisfying continuity, smoothness, shear, and moment balances.

The concentrated mass has no rotary inertia; however, the linear inertia of the mass must be accounted for. The boundary conditions imposed mathematically are therefore:

Table 4.2: Boundary conditions for a concentrated joint in a simulated waveguide.

Continuity:	$u\|_{x=0^-} = u\|_{x=0^+}$
Smoothness:	$u'\|_{x=0^-} = u'\|_{x=0^+}$
Moment balance:	$M\|_{x=0} = 0 \rightarrow EI\frac{\partial^2 u(0,t)}{\partial x^2} = 0$
Force balance:	$V\|_{x=0} = -m_j a \rightarrow EI\frac{\partial^3 u(0,t)}{\partial x^3} = m_j\frac{\partial^2 u(0,t)}{\partial t^2}$

The conditions shown in Table 4.2 translate into relationships between the various amplitude spectra in the two beam sections. These relationships can be solved at each frequency for the remaining unknown amplitude spectra $\hat{C}_1$, $\hat{D}_1$, $\hat{A}_2$, and $\hat{B}_2$. The total solution can then be assembled by plugging $\hat{A}_i, \hat{B}_i, \hat{C}_i$, and $\hat{D}_i$ into Eq. (2.8) and using the inverse Fourier transform to get the time-domain response of each section as a function of position and time.

Fig. 4.3a and Fig. 4.3b depict the global response of the simulated beam for a low and high frequency case; the incident wave can be seen traveling towards and reflecting off of the point mass in the center of the beam, and the reflections can then be seen traveling back towards the source of the wave. In an intermediate region near the point mass, the reflection and the incident wave overlap, whereas at parts of the beam further from the point mass the incident wave and reflection can be visibly separated in the time domain. Note how for lower frequency pulses, the reflections overlap with the incident wave sooner due to the longer wavelengths at low frequencies.

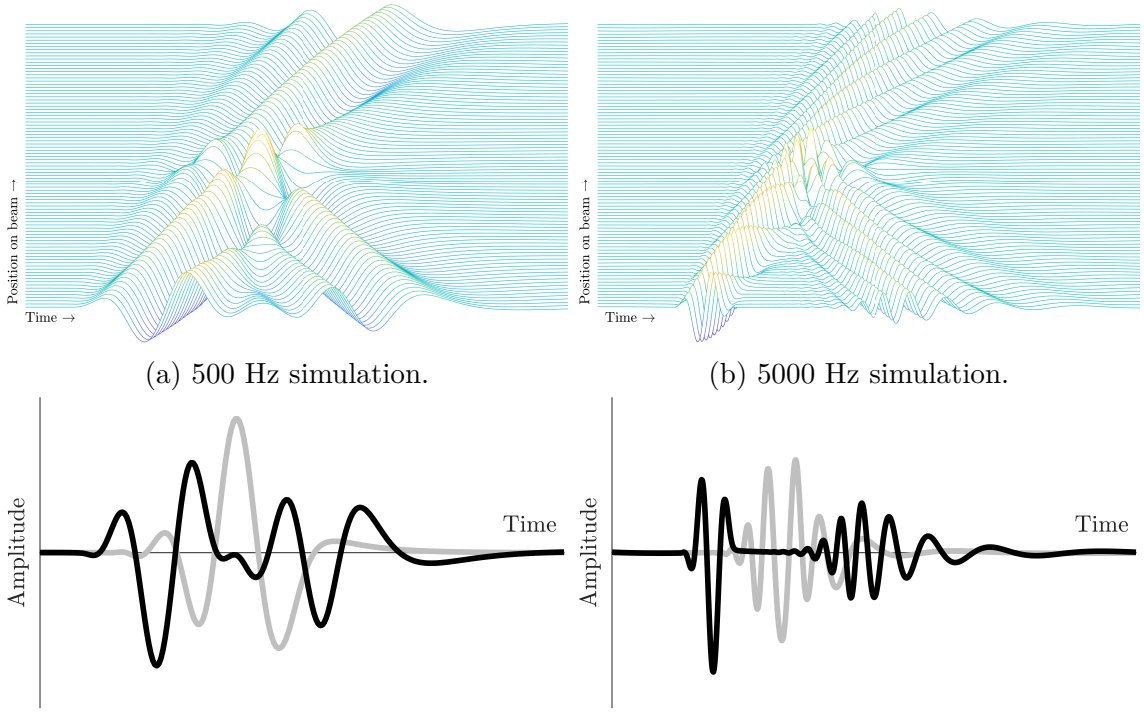

(a) 500 Hz simulation.

(b) 5000 Hz simulation.

(c) 500 Hz example measurements.

(d) 5000 Hz example measurements.

Figure 4.3: Simulated response to two-cycle toneburst with a reflection source at the center of the beam for two different frequency pulses.

The response of the beam is simulated for 6 center frequencies and 5 stress values. The center frequencies of 50, 100, 500, 1000, 2500, and 5000 Hz are selected somewhat arbitrarily in order to obtain good coverage of a wide range of the dispersion curve, and the 5 tensile stress values of 0, 5, 10, 15, and 20 MPa are used to match the stresses applied in the lab experiment. From the global response generated in the simulations, 8 local responses such as those in Fig. 4.3c and Fig. 4.3d are passed on as vibration measurements to the stress measurement algorithm.

4.2 Simulation results

The output of Algorithm 1 is the incident wave Fourier coefficients, the reflected wave Fourier coefficients, and the set of dispersion curve estimates. As can be seen in Fig. 4.4, the algorithm is able to separately identify both the incident and reflected wave. This is true both in the case of time-separable reflections, such as the 5000 Hz case shown in Fig. 4.4b, and also in the case where the reflection overlaps with the incident wave in the time domain, such as at low frequencies like the 500 Hz case shown in Fig. 4.4a.

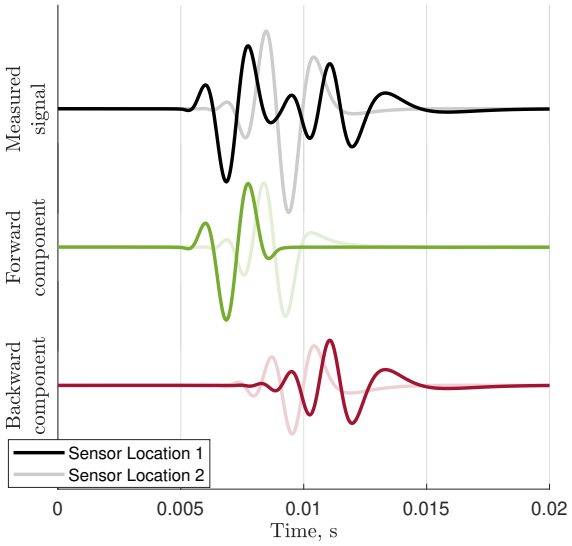

(a) Decomposed low-frequency signals (500 Hz).

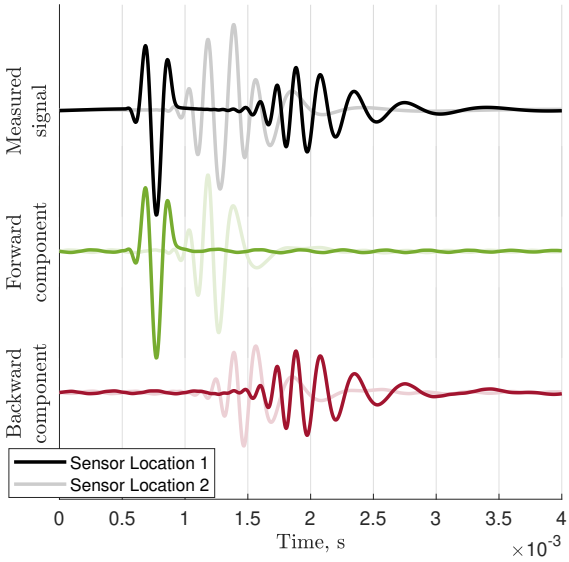

(b) Decomposed high-frequency signals (5000 Hz).

Figure 4.4: Decomposed incident and reflected waves from simulation test cases. Dark lines correspond to locations closer to the actuator source, whereas light lines correspond to locations farther from the wave source but closer to the reflection source. Note how the forward propagating incident wave passes by Sensor 1 first and then Sensor 2, whereas the backward propagating reflected wave passes Sensor 2 first before reaching Sensor 1.

The third output of Algorithm 1, and the output which contains the information about stress, is the estimated dispersion curve points. Fig. 4.5a shows the set of wavenumbers estimated for each frequency in the 50 Hz trial data. It is important to note that while the pulse has a center frequency of 50 Hz, it contains other frequency content besides 50 Hz as well (since it is a finite pulse and not an infinite sine wave). Thus, when we perform an FFT, each frequency component can be solved (individually). In Fig. 4.5a, each circle represents the wavenumber estimated for a particular frequency component, and the circle is darkened according to the confidence weighting given by the power spectral density of the input signal[2]. Note how for the estimates near the center frequency are given more credence. By combining many frequency trials throughout a selected frequency range of interest, we can construct an entire dispersion curve with high confidence, which is shown in Fig. 4.5b. It is evident that the stress (20 MPa in the case shown in Fig. 4.5) causes a deviation from the nominal unstressed dispersion curve.

Also shown in Fig. 4.5b is the result of fitting the analytical dispersion curve to the cumulative set of wavenumber estimates given by Algorithm 1. It can be seen that for a given simulated stress value, a good fit can be recovered by varying the stress parameter. Table 4.3 tabulates the results from fitting the 5 different simulated stress cases, and Fig. 4.6 displays the same information graphically. The algorithm is able to recover the prescribed stress to a reasonably high accuracy of within 1 MPa; for context, this amount of error corresponds to less than 1°F of error in measuring the neutral temperature of the structure, which is more than sufficient.

Since the different portions of the dispersion curve depend differently on the various material and geometry parameters, this algorithm can also be used to perform model updating to correct for deviations from nominal material and geometry properties simultaneously while

[2]The power spectral density of a signal `y` is given by `PSD = abs(fft(y)) .^ 2`. Since this is a weighting, we normalize `abs(fft(y))`, so `abs(fft(y)) .^ n` for any integer `n` all qualitatively have similar shapes, just that higher exponent values tighten the confidence band. The PSD corresponds to `n=2` and is selected since it physically pertains to the energy in the signal, but other `n` values could also be used.

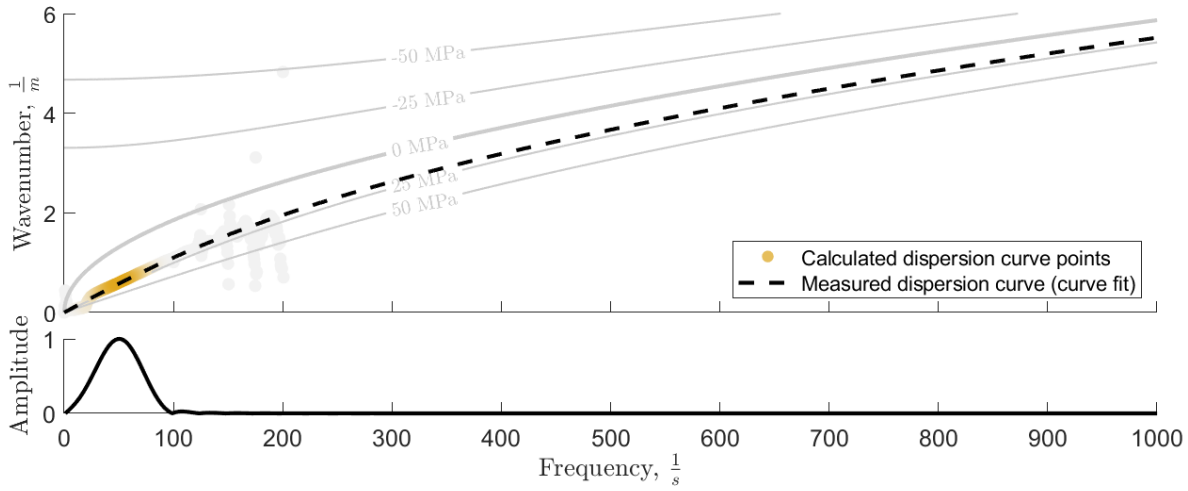

(a) Dispersion curve estimates from a single 50 Hz frequency trial.

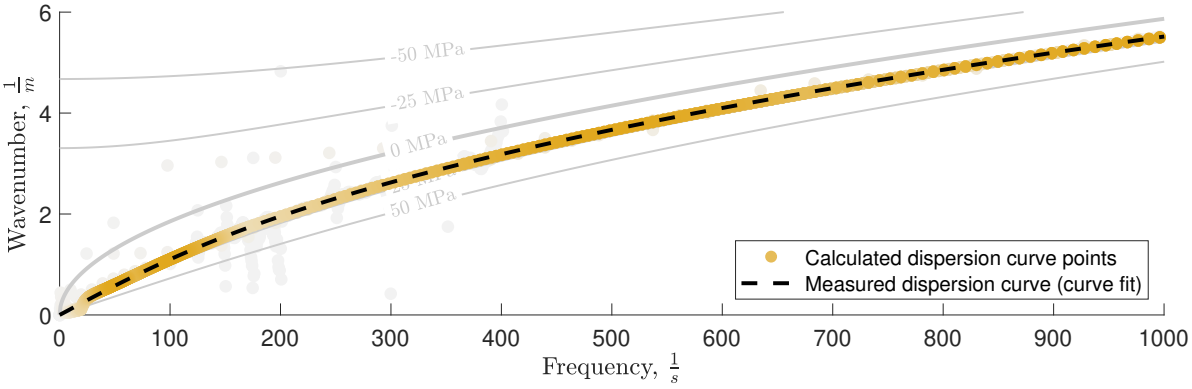

(b) Cumulative dispersion curve estimate from all 6 frequency trials.

Figure 4.5: Dispersion curve estimates for simulated test cases with 20 MPa of tensile stress; the wavenumber estimates at each frequency are colored darker according to the amount of energy for each frequency component. In the top figure, only a single trial at 50 Hz is used, hence the curve is only accurate near 50 Hz (which is shown by the color gradient). In the bottom figure, trial results from 50, 100, 500, 1000, 2500, and 5000 Hz are appended together to construct the entire dispersion curve over this range of frequencies.

Table 4.3: Summary of stress measurement results on simulated data.

True Stress	Calculated Stress
0 MPa	-0.7 MPa
5 MPa	4.3 MPa
10 MPa	9.3 MPa
15 MPa	14.4 MPa
20 MPa	19.5 MPa

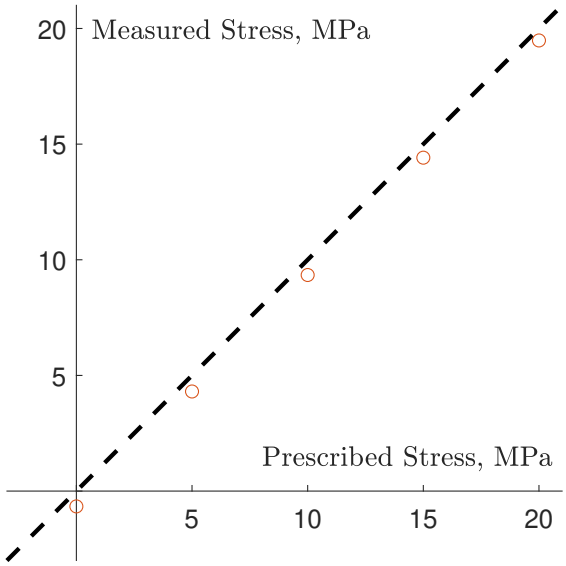

Figure 4.6: Stress estimated using wave propagation measurements vs. stress prescribed in the simulation. Ideally, if the measurements agree, they should fall along the diagonal.

measuring the stress. Consider a case where the elastic modulus, cross-sectional area, and density of the material are 80% of the nominal values. Fig. 4.7a shows the dispersion curve which is estimated by algorithm Algorithm 1 *only solving for stress*, and it can be seen that it deviates in the higher frequency portion compared to the nominal dispersion curve for the structure at the prescribed stress value.

Fitting not just the stress, but now also the material and geometry parameters (using the nominal values only as initialization points) allows the algorithm to perform both stress measurement and model updating all at once; this allows for correcting for uncertainties

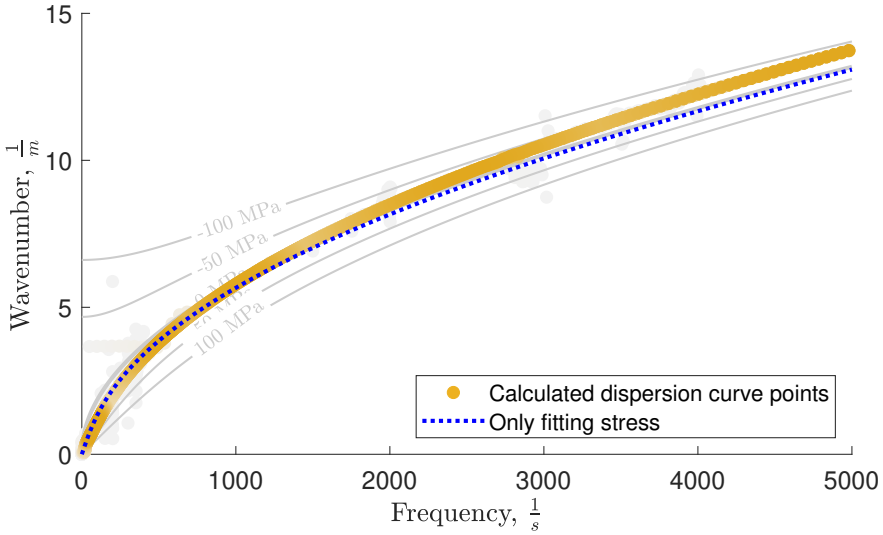

(a) Dispersion curve estimates showing deviation from nominal material and geometry curve.

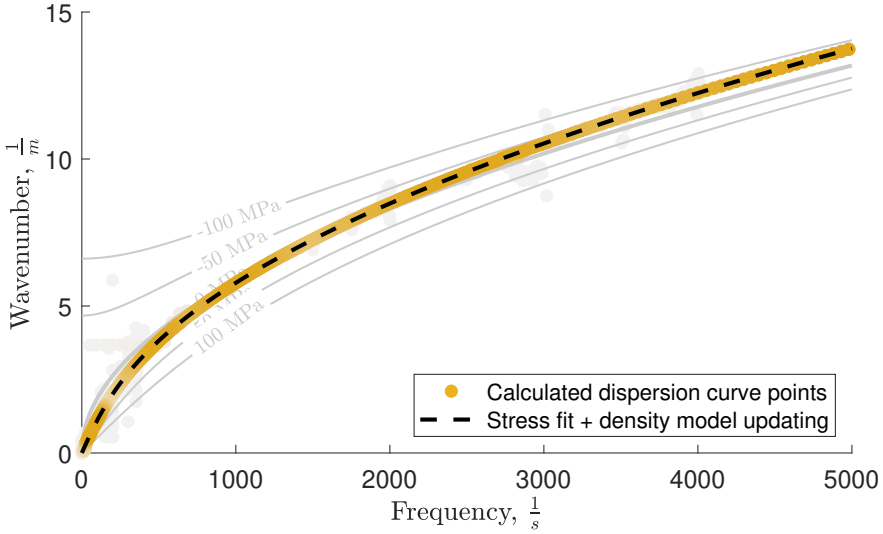

(b) Curve fitting the dispersion curve to both measure stress and perform model updating.

Figure 4.7: Demonstration of model updating to correct high-frequency portion of the dispersion curve while measuring stress. Note how despite the tensile stress, which should pull the curve beneath the zero-stress nominal dispersion curve, the high-frequency portion of the curve is shifted upwards due to the material/geometry values being off-nominal. In (a), this throws off the stress measurement, whereas in (b) the model updating feature accounts for this by fitting the density parameter as well.

in model parameters simultaneously while performing the stress measurement. Fig. 4.7b shows the effect of this model updating, which is effectively correcting for the deviation of the dispersion curve at high frequencies and allowing the stress to more accurately be determined from the low frequency portion of the curve.

4.3 Experimental setup

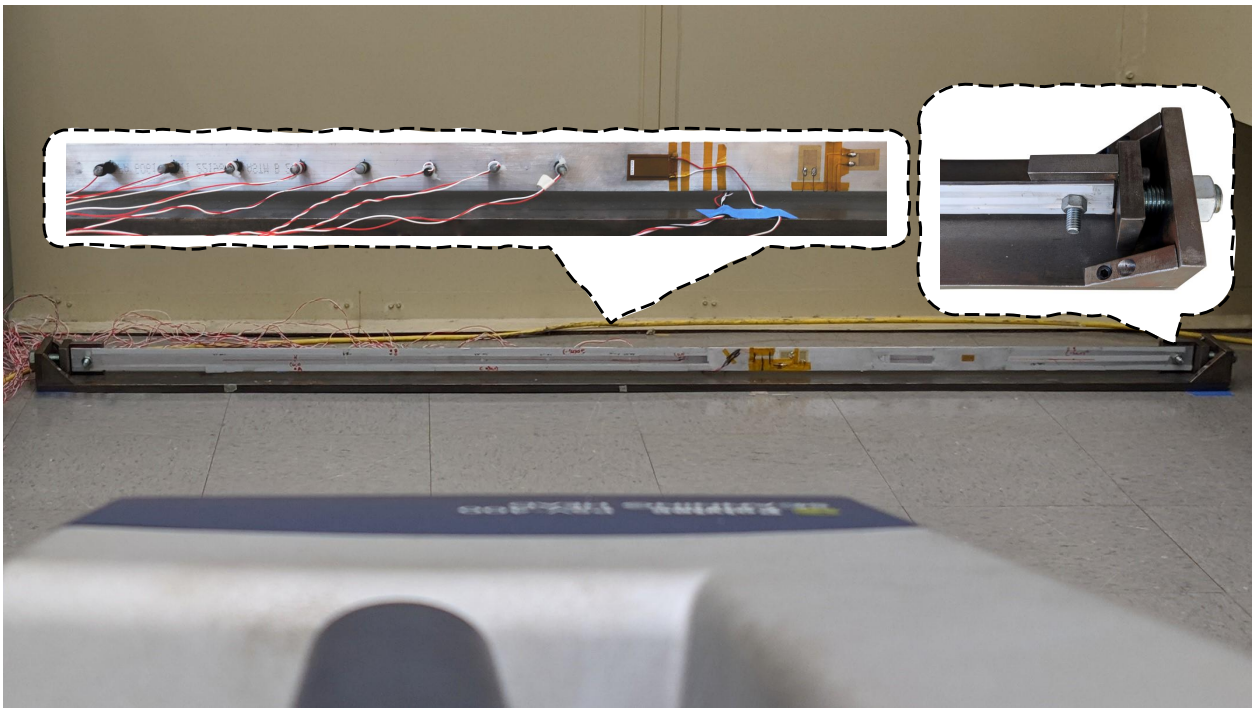

Figure 4.8: Experimental setup showing the view of the test article from the laser doppler vibrometer. The first callout shows the rear instrumented section with (from left to right) accelerometers, the MFC actuator, and strain gages. The second callout shows the tensioning mechanism which is present at both ends of the beam.

To validate the performance of the dispersion curve and subsequent stress measurement technique on real-world data, an experiment using the same beam tensioning rig used in [3] was conducted. The overall objective of the experiment was to validate the performance of the changes and improvements made to the stress measurement technique, specifically

regarding:

1. the ability to compensate for reflections
2. techniques for better dealing with random noise

In particular, these improvements were aimed at automating any manual processes in Albakri's original stress measurement technique, such as manually identifying and isolating the incident wave and manually initializing the optimization problem to ensure proper solution convergence.

The test article can be seen in Fig. 4.8, and it is the same article used in [3], consisting of an Aluminum 6061 rectangular beam obtained from McMaster-Carr with the following dimensions:

Table 4.4: Test article dimensions.

Geometry		
W	width	3.81 cm
T	thickness	3.175 mm
A	cross-section area	$W \cdot T$
I	cross-section moment of inertia	$\frac{1}{12} W \cdot T^3$
Material		
ρ	density	2700 kg/m^3
E	elastic modulus	69 GPa
ν	Poisson ratio	0.33

The waveguide properties of the test article are identical to the properties employed in the simulation results provided in Section 4.1. However, the boundary conditions of the test article are different from the boundary conditions prescribed in the simulation. In particular, the test article has both boundaries fixed, whereas the simulation contained a single reflection

source as a simplifying measure. Therefore, another goal of the experiment was to observe the performance of the reflection compensation aspect of the technique in the presence of multiple reflection sources. It should be noted, however, that the technique was developed to be boundary condition agnostic, so while the reflections themselves in the experiment may be different from the simulated cases, the code should be able to identify them all the same.

The beam tensioning rig (visible in Fig. 4.8) developed by Albakri et al. [3] consists of a steel beam with two end brackets mounted at either side. The end brackets have through-holes drilled, allowing a tensioning bolt to pass through each end. Attached to each tensioning bolt is a clamp mechanism for the test article; the test article is thus attached at both boundaries to a tensioning bolt which can be tightened to apply stress to the beam. Design choices such as the dimensions and materials of both the test article and the rig were made so that a reasonable amount of tension could be applied to the test article without buckling the tensioning rig, hence the test article was made out of aluminum while the rig was made out of much thicker and stiffer steel. The rig frame itself begins to exhibit a small amount of bending above 15 MPa of stress applied to the test article due to the asymmetric loading of the frame; however, it was determined that this bending was inconsequential for the purposes of the experiment. Nonetheless, no tension greater than 20 MPa of stress was applied to the test article for safety purposes.

Additionally, it is important to note that the rig is only capable of applying tensile stress to the test article; because of the material and geometry characteristics of the aluminum test beam, applying any amount of compressive stress immediately results in buckling of the test article.

A set of four Budd C40-161-350 strain gages with a nominal gage factor of 2.04 and a nominal gage resistance of 350 Ohms in a full-bridge configuration as seen in Fig. 4.9 are used to obtain a ground-truth measurement of the tensile stress applied to the beam.

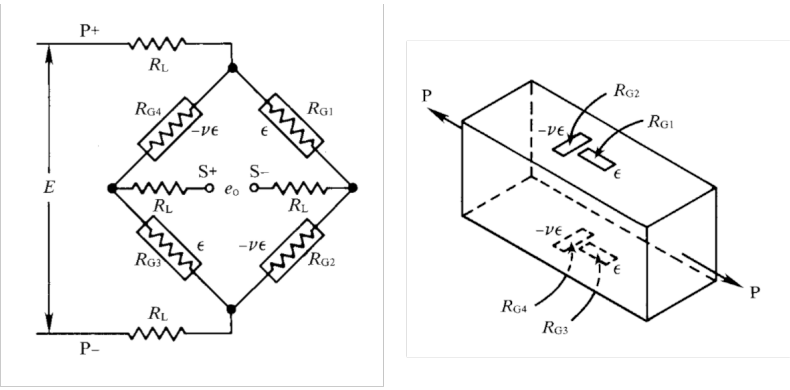

Figure 4.9: Full-bridge strain gage configuration for uniaxial stress, reproduced from [17].

Fig. 4.10 shows two of the four strain gages, whereas the other two are positioned on the back side of the beam.

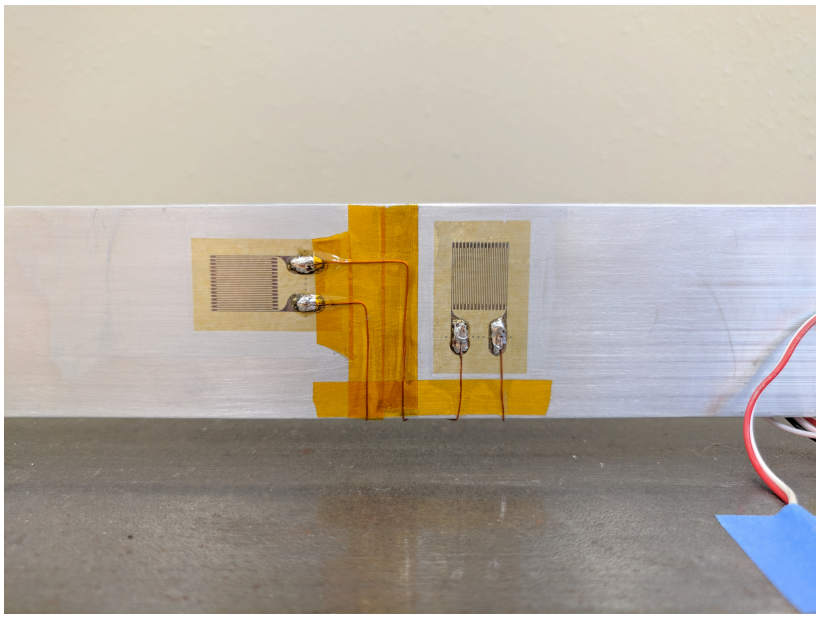

Figure 4.10: Photo of the strain gages used to measure the ground-truth stress in the beam.

As can be seen in Fig. 4.10, two of the strain gages are applied in the direction of the applied stress, whereas the other two are applied in the transverse direction to measure Poisson strains. This full-bridge configuration was selected to provide the maximal voltage output from the wheatstone bridge for the uniaxial stress state experienced by the beam [17].

A Hewlett Packard 6825A power supply was used to provide a 10 Volts supply voltage to the wheatstone bridge, and the output voltage across the measurement points bridge was measured using an NI 9232 data acquisition card.

To provide the excitation pulse for the wave propagation experiments, a Macro Fiber Composite (MFC) 2814 was adhered near the center of the beam; this location had been found to be optimal in [3] for minimizing reflection overlap, but in this work the location is not as critical. The MFC is oriented such that it expands and contracts primarily in the longitudinal direction of the beam; since it is attached to the side of the beam and displaced from the neutral axis, this expansion/contraction provides a bending moment that has been found to primarily actuate the stress-sensitive flexural modes of the beam (see Fig. 4.11). The actuator also will excite some longitudinal bar modes, as well as torsional modes due to any asymmetry in the placement of the actuator on the beam and any misalignment of the boundary clamps. However, these modes are considered small enough in amplitude to ignore in most cases.

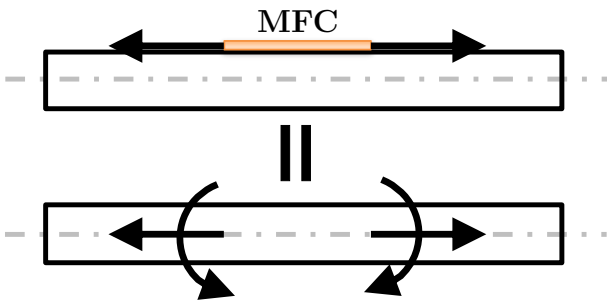

Figure 4.11: Free body diagram showing how an MFC actuator provides a bending moment to the beam.

The same 2-cycle sine wave modulated by a Hanning window as used in the simulations was generated in MATLAB and sent through an amplifier to the actuator using an NI 9263 analog voltage output DAQ card, and this output signal was also monitored using the NI 9232 as a reference signal. A Trek 50/750 high voltage amplifier with a gain set to 15 V/V

was used to amplify the signal to an amplitude of 150 Volts (zero to peak); this voltage was found to provide a good balance between signal level and signal quality, as overdrive distortion due to actuator nonlinearity became present at higher voltages.

Two types of vibration sensors were used in the experiment. The first set of sensors used in this experiment were PCB U352C67 Integrated Electronic Piezoelectric (IEPE) accelerometers[3], which provide high sensitivity while minimally mass-loading the test article. The eight accelerometer measurements were recorded using two NI 9234 DAQ cards in the IEPE configuration with AC coupling.

In addition to the accelerometers, a PSV-400 laser doppler vibrometer was used to obtain non-contact vibration measurements. This allowed for measuring the effect of mass-loading the structure with the accelerometers. It also allowed collecting a larger number of responses at more locations along the structure, which could be used to generate nice animations of the structure's response. 45 scan points over a span of approximately 100 cm from the actuator to one boundary were used, with a spacing of approximately 2 cm. The PSV-400 was equipped with a PSV-A-420 geometry scan unit in order to accurately measure the locations of the scan points on the beam. The PSV-400 was triggered using the same excitation voltage sent to the actuator.

The NI 9232, 9234 and 9263 DAQ cards used for measuring the strain gage, accelerometers, and sending the excitation signal, respectively, were housed in an NI cDAQ-9184 4-Slot chassis, which was connected via ethernet to a Windows 10 laptop with an AMD Ryzen 9 5900HS CPU, 16GB Ram, Nvidia RTX 3070 GPU and controlled using MATLAB 2021a. The NI DAQ's floating ground was connected to common ground using a jumper between the NI DAQ's ground lug and a common ground on the HP amplifier, whereas all of the

[3]Each accelerometer was individually calibrated prior to the experiment using a handheld PCB 394C06 1 g calibration shaker

other components were all connected to common ground through their 3-prong power plugs.

Because the experiment required sending pulses over a wide range of center frequencies, the sampling rate for the DAQ was updated adaptively depending on the center frequency of each pulse in order to obtain consistent sampling between different frequency trials. The NI 9232 and 9234 DAQ cards contain an internal master clock with a frequency of 13.1072 MHz, requiring sampling at a rate provided by

$$f_s = \frac{13.1072 \div 256}{n}$$

where n is any integer between 1 and 31. In order to obtain at least 20 samples per waveform, which is sufficient to capture the frequency content of interest without over or under sampling, the following line of MATLAB code is used to determine the appropriate value for n for this application:

```
n = floor(13.1072*1e6/(256*20*centerFreq));
```

where the variable `centerFreq` is the center frequency of the wave pulse. The PSV-400 sampling frequency was selected to be as close as possible to the values used for the accelerometers, thought the data is not processed together so it is not critical to be synced. The selection of sampling time on the other hand is not trivial; for low frequencies in particular where standing waves can form, the optimal time to truncate the response is not obvious. That is, the structure's response does not die out after the initial wave or reflections pass; rather, it continues ringing, so it is not clear when the optimal time to stop recording the response would be. In the experiments presented here, the sampling time was selected to be 10 times the length of the excitation pulse.

The combination of the NI DAQ with accelerometers was selected primarily to allow for

flexibility of running the experiment automatically, whereas the PSV-400 required more manual input for running the various frequency cases.

In order to minimize the effects of random noise, the techniques of frequency diversity and time diversity are employed in the test execution; both are aimed at increasing the amount of confidence in the measurements by increasing the number of measurements. To account for possible spurious signals in the time domain, along with random noise from thermal noise and other sources, each measurement is repeated multiple times and averaged together. This assumes the response is repeatable, which is true in this case since the excitation is identical and synced for each run. The signal to noise ratio of the measurement after time averaging increases by a factor of $\sqrt{n}$, where n is the number of time averages taken.

Meanwhile, there may be particular frequencies which are more susceptible to interference from random noise sources, coherent noise such as unwanted wave modes, or other unforeseen hindrances. In order to make the method more robust against these frequency-specific sources of error, the technique of frequency-diversity is employed. Rather than performing a test using a single toneburst of a particular center frequency, we thus send pulses of various frequencies to fill out an entire frequency range. This also enables measuring a wider range of the dispersion curve, which can subsequently aid in the curve-fitting process.

In order to perform n runs at each of m frequency trials, the test is automated using MATLAB; this allows running the $n \times m$ measurements in a more efficient and less error-prone manner. For the experiments in this thesis, accelerometers measurements are averaged 36 times, whereas the laser vibrometer measurements are averaged 3 times. The frequencies selected for testing are 100, 150, 200, 250, 300, 400, 500, 750, 1000, 1250, 1500, 2000, 2500, 3000, 4000, and 5000 Hz. This frequency selection has not been optimized, and was simply selected to give good coverage over a range of 0 to 5 kHz. Finally, using the tensioning rig and strain gage for reference, the beam is prescribed stresses of 0, 5, 10, 15, and 20 MPa.

4.4 Experimental results

First, let us consider the experimental results using a laser vibrometer with no accelerometers. As with the simulated cases, the collection of sensor data from various frequency trials at a particular stress value is passed into algorithm Algorithm 1 in order to decompose the reflections and identify the dispersion curve, currently only solving for stress since the beam's material and geometry properties are known. Unlike the simulations, however, the experiment contains two boundaries, resulting in reflections coming from either direction. Fig. 4.12 shows the decomposed vibration signals from two sensor locations for a center frequency of 400 Hz.

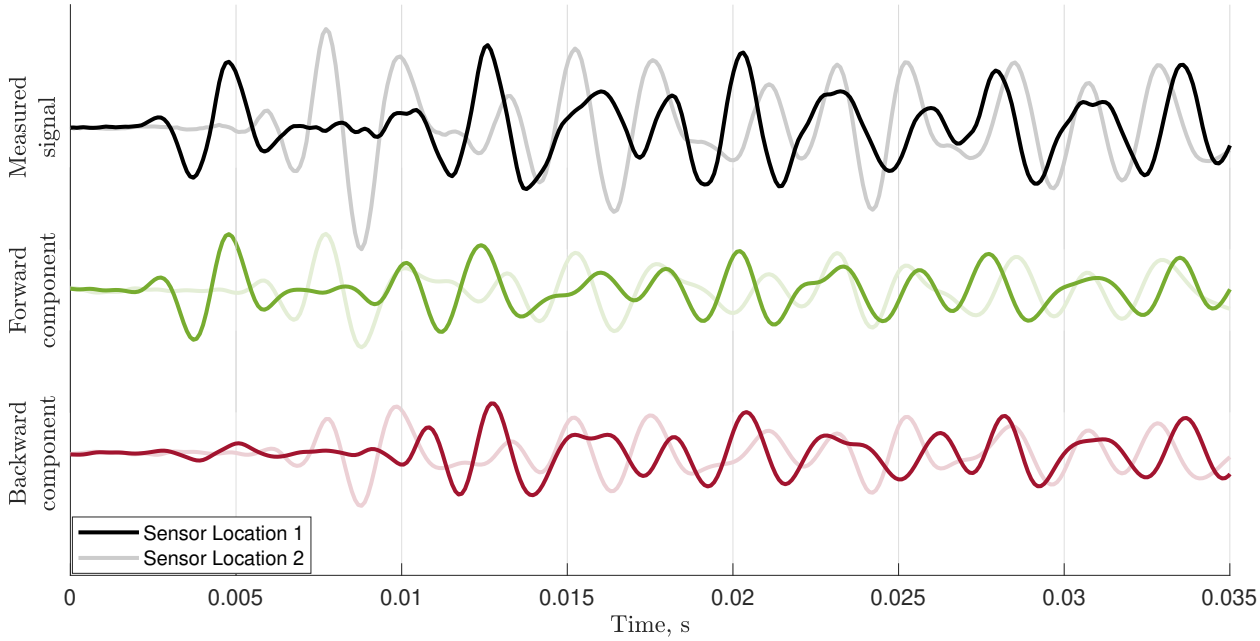

Figure 4.12: Decomposition of measurements into forward and backward propagating components; note that while only two sensor locations are shown, the algorithm requires at least three measurements to solve for the forward component, backward component, and dispersion curve. In this case, 45 laser vibrometer measurements were used to solve in a least-squares sense.

In the simulated case, one could characterize the decomposed signals as an incident wave

and a reflected wave; in the experimental data, the results are instead better characterized as a forward and backward propagating component of the signal. Recall again the theoretical total solution (Eq. (2.8)) for a Timoshenko beam:

$$u(x,t) = (\hat{A}e^{-ik_1 x} + \hat{B}e^{-ik_2 x} + \hat{C}e^{ik_1 x} + \hat{D}e^{ik_2 x})e^{i\omega t}$$

If there are multiple wave modes with the same wave number propagating in the same direction, their Fourier coefficients will add together to form a cumulative wave; indeed, the cumulative wave has an infinite number of decompositions which are not unique. Thus, when the algorithm solves for the 'incident' and 'reflected' waves' Fourier coefficients, it really is solving for the cumulative wave corresponding to the forward or backward propagating wavenumber. Since the experimental beam has boundaries on either side, reflections will alternate between propagating forward and backwards; this is seen in the decomposition as multiple appearances of pulses in the two decomposed signals. Further effort could be expended trying to separate the various reflections from the original signal, but this has little impact on the problem at hand of measuring stress and would require additional knowledge about the boundary conditions.

Nonetheless, knowing the experimental setup, we can identify the various pulses visible in the decompositions for curiosity's sake. First, we see the traditional 'incident wave' appearing in the measured signal near 0.005 seconds and identified as a forward propagating component. Next, however, when we might expect to subsequently only see a reflected wave propagating backwards around 0.0125 seconds, we also see another forward propagating pulse. A component which has until now been ignored is the *backwards* incident wave; that is, at the moment of excitation, the actuator sends pulses symmetrically forward and backwards. When this initially backward propagating component hits the back boundary, it is reflected and begins to propagate forwards. Thus, since the actuator is near the center

of the beam, around the time that the traditional 'reflected' wave appears, so too will the reflected *backwards* wave. Depending on the actuator and sensor placements, which reflection arrives first may vary, or they may appear to arrive at the same time.

Subsequently, one can see reflections of reflections appearing, for example at the 0.02 second mark; that is, the initially forward propagating 'incident' wave, reflected off of one boundary, and then reflected off of the other boundary to again propagate forwards. Similarly, the previously ignored 'backwards' incident wave will reflect off of the back and then off of the front to again travel backwards. These pulses can be seen as a third blip in the original time signal.

It is noteworthy that these results are attained without any significant pre-processing of the data; the time responses have not been filtered or windowed in any way in order to prevent leakage in the frequency domain. This data is the result of simply truncating the time response after 10 pulse-widths worth of data. For the case of very little damping as seen in this experiment, this means that the response is almost certainly and unavoidably truncated during a non-zero portion of the signal, the effects of which need to be investigated further[4].

For the purposes of measuring stress, what is more important than the decomposed signal is the estimated dispersion curve. The cumulative dispersion curves from all of the frequency trials for two of the five prescribed stress values are shown in Fig. 4.13. While there is some variation and error along the curve, the abundance of data due to the frequency-diversity principle helps to overcome this.

[4]recall that the FFT algorithm has implicit assumptions about the periodicity of the signal

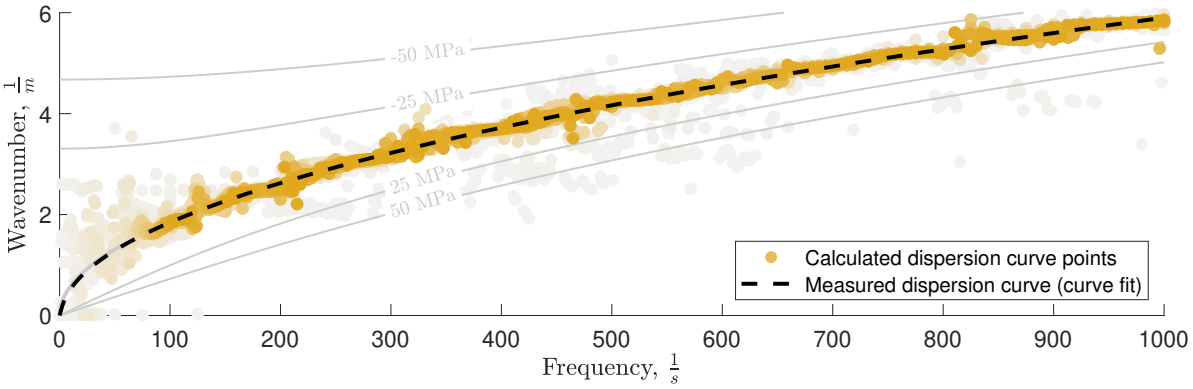

(a) Neutral stress dispersion curve.

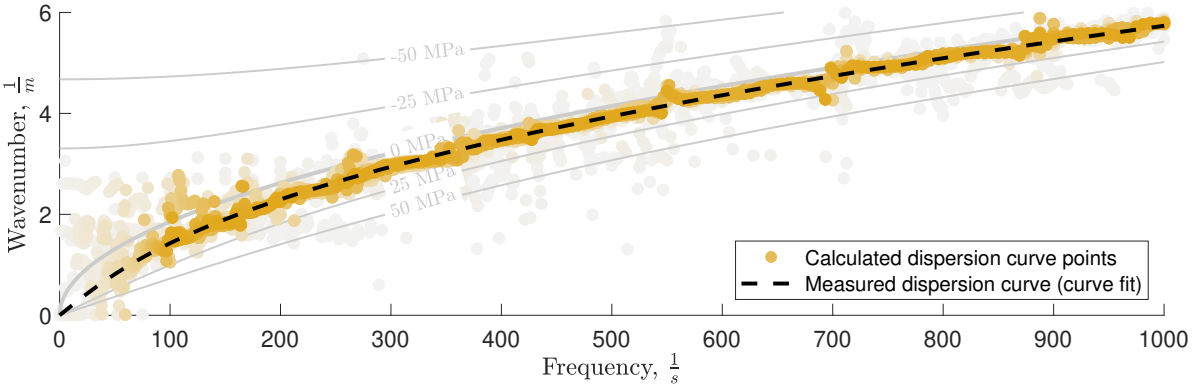

(b) 10 MPa tensile stress dispersion curve.

Figure 4.13: Curve fitting of the dispersion curve estimates to measure stress, laser vibrometer data. Recall that the circles are colored darker yellow according to the confidence obtained according to the PSD of input signal.

Performing the dispersion curve-fitting in order to measure stress in each different stress case gives the following results, where ± denotes the 95% confidence interval as obtained using MATLAB's curve-fitting toolbox `fit()` function:

Table 4.5: Summary of stress measurement results from fitting the dispersion curves.

True Stress	Laser Vib.
0 MPa	0.4 ± 0.1 MPa
5 MPa	3.6 ± 0.1 MPa
10 MPa	8.9 ± 0.1 MPa
15 MPa	13.1 ± 0.2 MPa
20 MPa	18.0 ± 0.2 MPa

These results can be plotted as shown in Fig. 4.14; ideally, if the ground truth stress using the strain gage circuit matches the 'measured' stress using the wave propagation measurements, the data should fall perfectly on the diagonal. A slight systematic under-prediction is visible in the measured stress, which is consistent with the results on simulated data.

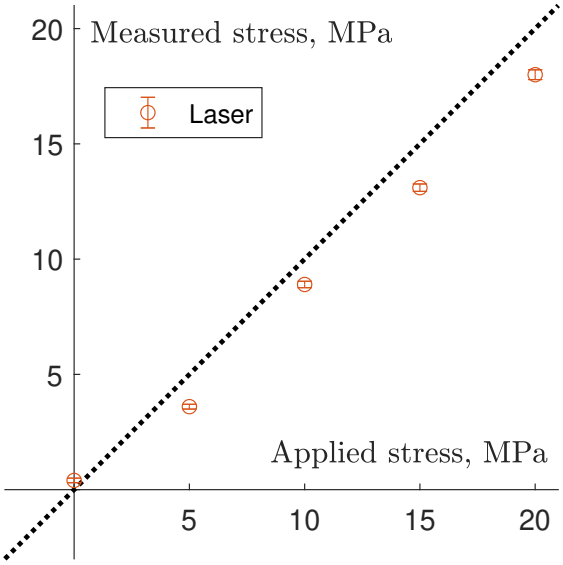

Figure 4.14: Stress estimated using wave propagation measurements vs. stress calculated using a strain gage. Ideally, if the measurements agree, they should fall along the diagonal.

It is possible that excluding the evanescent modes is the source of this error; nonetheless, the

estimated stresses are still within a few megapascals, which is considered sufficient since this translates to less than 1°F regarding neutral temperature, so no further effort was expended investigating this error. It is noteworthy that these results are on par with the *best-case*[5] results in Albakri et al. [3], which are the result of laborious manual pre-processing, selecting optimal data, and picking the best results from various frequency trials.

Next, let us consider the tests conduced with accelerometers placed on the beam, but still considering the laser vibrometer measurements. The dispersion curve estimates obtained from this dataset exhibit a deviation at higher frequencies from the nominal dispersion curve and from the dispersion curve measured without the accelerometers, as shown in Fig. 4.15.

This deviation is due to the mass loading of the accelerometers. Using some physical intuition, one might expect that the mass loading of the accelerometers would manifest in the density parameter for the waveguide, ρ. Accordingly, when we perform the curve fitting of the dispersion curve estimates, we can set the density as an additional regression parameter, along with the stress. Doing so demonstrates the ability of the technique to perform 'model updating' simultaneously with the stress measurement in order to account for uncertainties in the material and geometry properties. Fig. 4.16 shows the best-fit dispersion curve with the additional model updating for density for a stress value of 10 MPa.

The results of fitting the dispersion curve for all of the stress values with model updating are summarized in Table 4.6 and plotted in Fig. 4.17.

The need for performing model updating is clear here, as errors in the model parameters can result in errors in the stress measurement. However, the success of the model updating component of the regression is also demonstrated, as simply allowing the density to vary brings the stress measurement almost exactly in agreement with the tests conducted without accelerometers.

[5] In the worst-case results presented in [3], the error is on the order of 20 MPa.

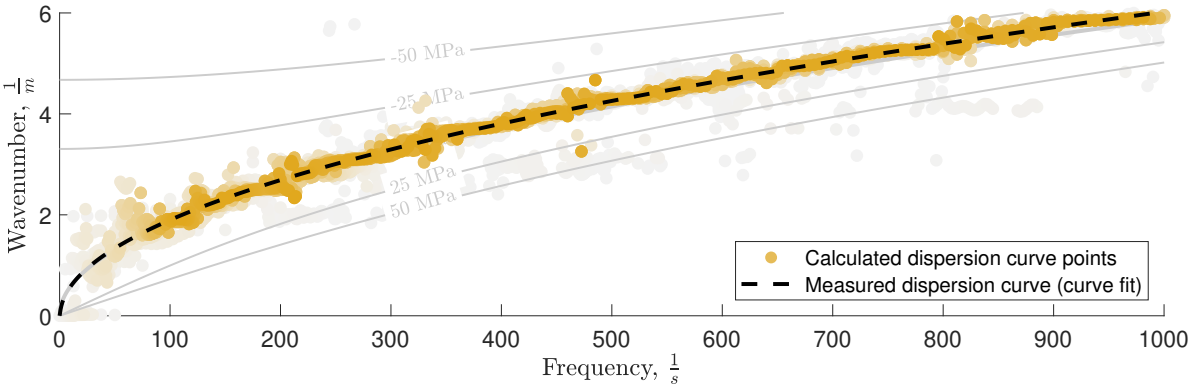

(a) Neutral stress dispersion curve.

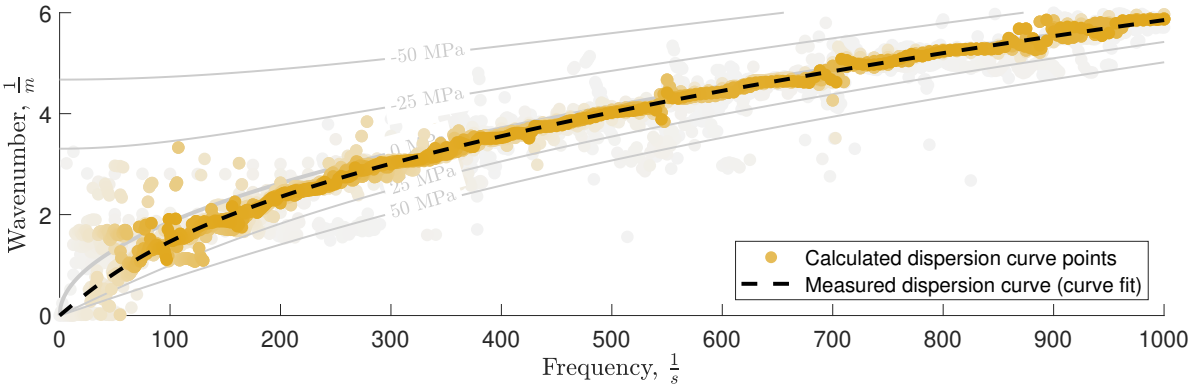

(b) 10 MPa tensile stress dispersion curve.

Figure 4.15: Curve fitting of the dispersion curve estimates to measure stress, laser vibrometer data with accelerometers attached to provide mass-loading disturbance.

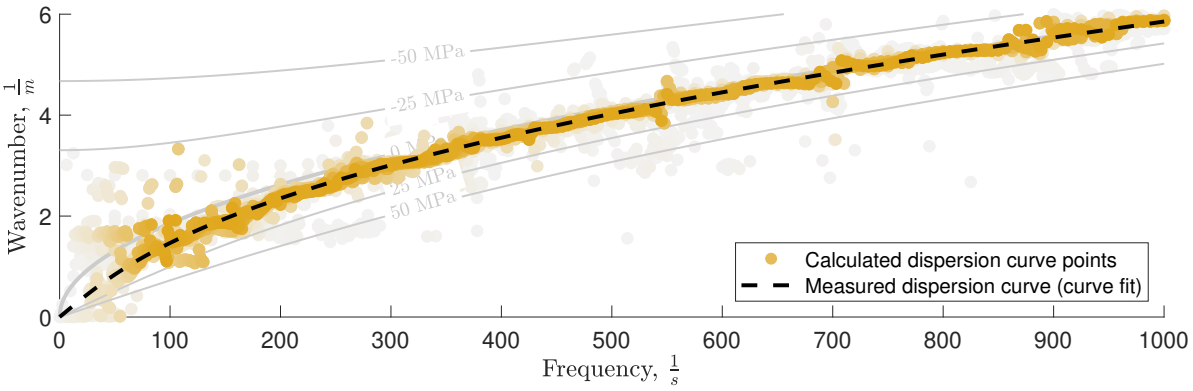

Figure 4.16: Model updating to correct for accelerometer mass loading.

Table 4.6: Summary of stress measurement results from fitting the dispersion curves from the laser vibrometer cases with and without accelerometer mass-loading.

True Stress	Laser Vib.	Laser Vib. w/ Accels
0 MPa	0.4 ± 0.1 MPa	0.1 ± 0.1 MPa
5 MPa	3.6 ± 0.1 MPa	3.5 ± 0.1 MPa
10 MPa	8.9 ± 0.1 MPa	8.9 ± 0.2 MPa
15 MPa	13.1 ± 0.2 MPa	12.6 ± 0.2 MPa
20 MPa	18.0 ± 0.2MPa	17.4 ± 0.2 MPa

Finally, consider the accelerometer measurements themselves. Unlike the laser vibrometer, which gave the response at a total of 45 locations, only 8 accelerometers are used; however, this is still more than the theoretical requirement of three measurements. As in the previous cases, the algorithm decomposes the signal into its forward and backward propagating components and gives the corresponding dispersion curve. Since the accelerometers are known to mass-load the structure, we solve for density parameter during the curve fitting process in order to perform model updating while also solving for the stress. Fig. 4.18 shows the dispersion curve estimates for the accelerometer measurements; there is higher variance and error, though this is expected since only 8 sensors are used as opposed to the 45 scan points used by the laser.

The results summarized in Table 4.7 and plotted in Fig. 4.19 compare all three test cases

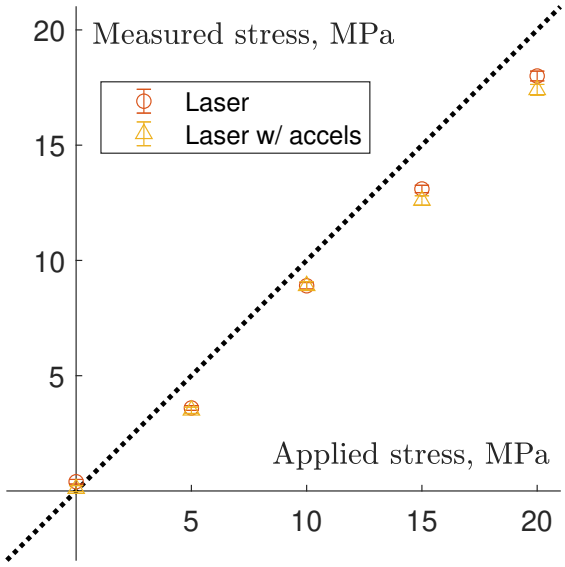

Figure 4.17: Stress estimated using wave propagation measurements vs. stress calculated using a strain gage. Ideally, if the measurements agree, they should fall along the diagonal.

presented. While the higher variance in the accelerometer data does translate to higher error and a wider 95% confidence interval for the stress measurements, the results are still within the tolerances required for the application of measuring neutral temperature. Although the error bounds are fairly tight, it is notable that the correct stress measurement does fall outside of the 95% confidence interval for many of the test cases.

Table 4.7: Summary of stress measurement results from fitting the dispersion curves.

True Stress	Laser Vib.	Laser Vib. w/ Accels	Accels
0 MPa	0.4 ± 0.1 MPa	0.1 ± 0.1 MPa	-1.1 ± 0.5 MPa
5 MPa	3.6 ± 0.1 MPa	3.5 ± 0.1 MPa	1.9 ± 0.5 MPa
10 MPa	8.9 ± 0.1 MPa	8.9 ± 0.2 MPa	8.8 ± 0.7 MPa
15 MPa	13.1 ± 0.2 MPa	12.6 ± 0.2 MPa	13.4 ± 0.6 MPa
20 MPa	18.0 ± 0.2MPa	17.4 ± 0.2 MPa	18.0 ± 0.8 MPa

Most importantly, all of the stress measurements are in good agreement with each other and with the ground truth based on the strain gage. While the geometry and material properties change between this structure and a rail, it is noteworthy that the accuracy

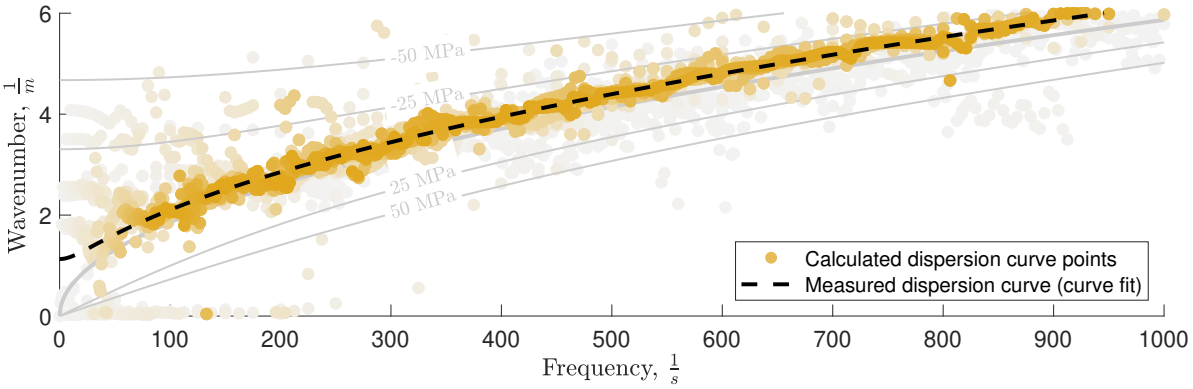

(a) Neutral stress dispersion curve.

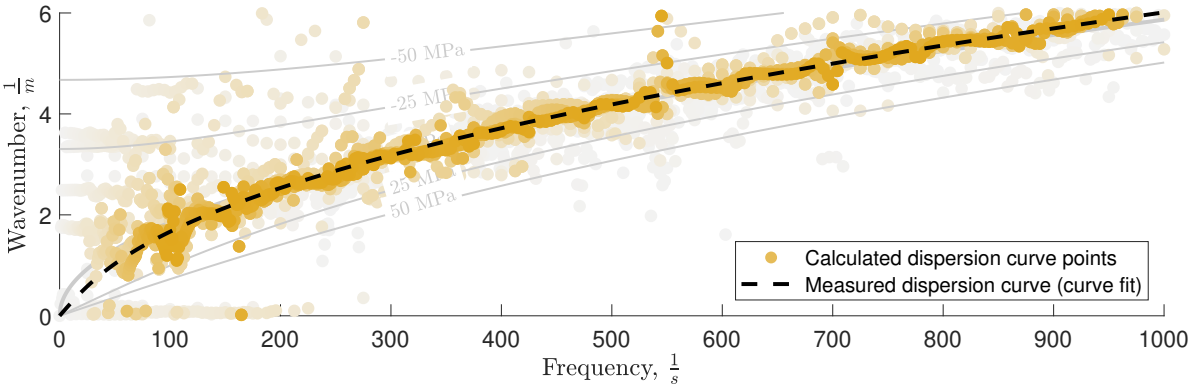

(b) 10 MPa tensile stress dispersion curve.

Figure 4.18: Curve fitting of the dispersion curve estimates to measure stress.

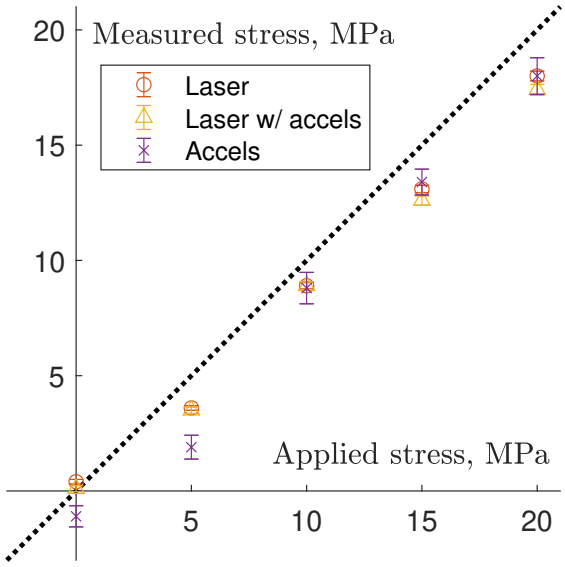

Figure 4.19: Stress estimated using wave propagation measurements vs. stress calculated using a strain gage. Ideally, if the measurements agree, they should fall along the diagonal.

obtained here is sufficient to estimate neutral temperature to within 1°F, which demonstrates the success of the technique. Furthermore, the technique is able to handle material and geometry uncertainty, here demonstrated by the ability to compensate for accelerometer mass-loading, and it is indifferent to boundary conditions because of its ability to decompose reflections.

Chapter 5

Conclusions and Future Work

A new technique for identifying the forward and backward propagating components of a signal, along with the corresponding dispersion curve, has presented and applied to the problem of non-destructively measuring stress in a beam. The underlying principle that the vibration characteristics of the structure are dependent on the stress is well known, but the additional dependencies of the vibration characteristics on material, geometry, and boundary conditions have limited techniques in the past.

While boundary conditions in principle do not affect wave propagation, mode conversion, primarily in the form of reflections at the boundaries, give rise to a coherent noise source which has previously been a major limitation of related works. In this work, a boundary condition agnostic approach is developed in which the wave is simply decomposed in the frequency domain into the forward and backward propagating components of the signal. The Fourier coefficients of the various wave modes at each frequency appear simply as a linear sum in the theoretical formulation. Interpreting the Fourier coefficients as vectors in the complex plane, the problem of solving for the forward and backward propagating components of the signal becomes a relatively straightforward 'vector addition problem', giving rise to a nonlinear system of equations which are solved for the various wave modes and their dispersion curves.

Ultimately, a Timoshenko beam model is fitted to the estimated dispersion curve in order to obtain a measurement of the stress; simultaneously, additional material and geometry

parameters can be solved for as a 'model updating' feature.

The developed theory is validated in an experiment using a rectangular aluminum beam with a tensioning device to apply different values of stress. An automated test is devised which measures wave pulses at various frequencies in order to measure the entire dispersion curve. Measurements are time-averaged in order to reduce the effects of random noise, whereas different excitation frequencies are used to counteract frequency-dependent coherent noise sources.

The results of the experiments show the successful decomposition of signals into forward and backward propagating components, including cases where the reflections completely overlap and begin to form standing waves. Furthermore, the model-updating feature is successfully able to correct for mass-loading from accelerometers, demonstrating the ability of the method to account for material and geometry uncertainty. The stress measurements are ultimately found to be sufficiently accurate for the desired application of measuring rail neutral temperature. Despite a small systematic under-prediction of stress, the various tests were in agreement with each other, and it is estimated that the level of error in the stress measurements would translate to less than 1°F of error in measuring neutral temperature.

Future Work

The immediate next step for this work is to attempt in-field implementation to measure rail neutral temperature on a full-sized railroad. This test is scheduled to be conducted at TTCI in Pueblo, Colorado in mid August of 2021. Preliminary testing has suggested that the piezoelectric actuators used in this work provide insufficient force at the frequencies required to measure stress in a rail. A fixture which would permit using an electrodynamic shaker, which can produce higher forces at lower frequencies than piezoelectric actuators, has thus

been built and will be tested during this field test. This fixture would permit the appropriate flexural wave mode to be excited using the electrodynamic shakers rather than piezoelectric actuators.

In addition to investigating other excitation solutions, various sensor solutions should be investigated for use in the field. While accelerometers have been preferred due to their relative affordability, it is possible that the ability to measure the response over a larger spatial domain, or at more locations along the rail, could improve robustness in the field. Thus, future work should also investigate the benefits of using a laser vibrometer or other measurement systems.

With appropriate actuators and sensors for use on in-field rail, the technique presented in this thesis represents a very promising step towards a reliable reference-free system for non-destructive rail stress and neutral temperature measurement.

Additional applications

While this work was motivated by the problem of rail neutral temperature, the developed technique can easily be applied to other applications in which stress in beams must be measured non-destructively. However, the extension of this work to plates and shells would open up a much wider range of applications, especially in aerospace settings. Furthermore, while this work was mainly aimed at stress measurement, applications to measuring stiffness, density, or other material and geometry properties should also be investigated.

The underlying signal processing technique regarding the identification and separation of forward and backward propagating signals in measurements also has other potential applications. One such extension of this work includes footstep localization in buildings, in which vibration signals propagating through floors can be analyzed to locate pedestrians.

Bibliography

[1] Donald R. Ahlbeek and James M. Tuten. Rail Neutral Temperature Test on CSX. Technical report, Federal Rail Administration, Columbus, Ohio, 1990.

[2] Mohammad I. Albakri and Pablo A. Tarazaga. A novel acoustoelastic-based technique for stress measurement in structural components. *Conference Proceedings of the Society for Experimental Mechanics Series*, 2(1):49–56, 2016. ISSN 21915652. doi: 10.1007/978-3-319-29751-4_7.

[3] Mohammad I. Albakri, V. V.N.Sriram Malladi, and Pablo A. Tarazaga. Low-frequency acoustoelastic-based stress state characterization: Theory and experimental validation. *Mechanical Systems and Signal Processing*, 112:417–429, November 2018. ISSN 10961216. doi: 10.1016/j.ymssp.2018.04.011.

[4] Mohammad I. Albakri, Vijaya V.N. Sriram Malladi, Serkan Gugercin, and Pablo A. Tarazaga. Estimating dispersion curves from Frequency Response Functions via Vector-Fitting. *Mechanical Systems and Signal Processing*, 140:106597, 2020. ISSN 10961216. doi: 10.1016/j.ymssp.2019.106597. URL https://doi.org/10.1016/j.ymssp.2019.106597.

[5] Ivan Bartoli, Francesco Lanza Di Scalea, Mahmood Fateh, and Erasmo Viola. Modeling guided wave propagation with application to the long-range defect detection in railroad tracks. *NDT&E International*, 38:325–334, 2005. ISSN 09638695. doi: 10.1016/j.ndteint.2004.10.008.

[6] Nihat Mustafa Bilgutay. *Split-Spectrum Processing for Flaw-to-Grain Echo Enhancement in Ultrasonic Detection*. Phd thesis, Purdue University, 1981.

[7] Thomas P. Boggs. *Determination of axial load and support stiffness of continuous beams by vibration analysis*. PhD thesis, Virginia Tech, October 1994. URL https://vtechworks.lib.vt.edu/handle/10919/45623.

[8] Anna Castellano, Aguinaldo Fraddosio, Salvatore Marzano, and Mario Daniele Piccioni. Some advancements in the ultrasonic evaluation of initial stress states by the analysis of the acoustoelastic effect. *Procedia Engineering*, 199:1519–1526, 2017. ISSN 18777058. doi: 10.1016/j.proeng.2017.09.494. URL http://dx.doi.org/10.1016/j.proeng.2017.09.494.

[9] Paul Chinowsky, Jacob Helman, Sahil Gulati, James Neumann, and Jeremy Martinich. Impacts of climate change on operation of the US rail network. *Transport Policy*, 75 (March 2017):183–191, 2019. ISSN 1879310X. doi: 10.1016/j.tranpol.2017.05.007. URL https://doi.org/10.1016/j.tranpol.2017.05.007.

[10] CNN. Why Chicago train tracks are being set on fire, 2019. URL https://www.cnn.com/videos/weather/2019/01/30/chicago-train-tracks-fire-newsource-orig.cnn.

[11] Vesna Damljanović and Richard L. Weaver. Laser vibrometry technique for measurement of contained stress in railroad rail. *Journal of Sound and Vibration*, 282(1-2): 341–366, 2005. ISSN 0022460X. doi: 10.1016/j.jsv.2004.02.055.

[12] James F. Doyle. *Wave Propagation in Structures-Spectral Analysis Using Fast Discrete Fourier Transforms*. Springer, second edition, 1997. ISBN 1461273048.

[13] D. M. Egle and D. E. Bray. Measurement of acoustoelastic and third-order elastic constants for rail steel. *Journal of the Acoustical Society of America*, 60(3):741–744, 1976. ISSN NA. doi: 10.1121/1.381146.

[14] Charles R. Farrar and Keith Worden. An introduction to structural health monitoring. *Philosophical Transactions of the Royal Society A: Mathematical, Physical and Engineering Sciences*, 365(1851):303–315, 2007. ISSN 1364503X. doi: 10.1098/rsta.2006.1928.

[15] Robel Bahnbaumaschinen GmbH. Rail pulling devices - Tools and small machines, 2021. URL https://www.trackopedia.info/encyclopedia/maintenance-of-way/tools-and-small-machines/rail-pulling-devices.

[16] S. Gokhale and S. Hurlebaus. Monitoring of the stress free temperature in rails using the acoustoelastic effect. *AIP Conference Proceedings*, 975(2008):1368–1373, 2008. ISSN 0094243X. doi: 10.1063/1.2902594.

[17] Vishay Precision Group. Shunt Calibration of Strain Gage Instrumentation. Technical report, Vishay Precision Group, 2013. URL www.micro-measurements.com.

[18] Viktor Hauk. *Structural and Residual Stress Analysis by Nondestructive Methods*. Elsevier, 1997. ISBN 0 444 82476 6 9.

[19] Scott Hendricks. *Dynamics III: Vibrations Lecture Notes*. Virginia Tech, Department of Engineering Science and Mechanics, Blacksburg, Virginia, 2018.

[20] D. S. Hughes and J. L. Kelly. Second-Order elastic deformation of solids. *Physical Review*, 92(5):1145–1149, December 1953. ISSN 0031899X. doi: 10.1103/PhysRev.92.1145. URL https://journals.aps.org/pr/abstract/10.1103/PhysRev.92.1145.

[21] Committee on Nondestructive Testing of Longitudinal Force in Rails. Prediction of Rail Buckling: Recommendations for Development of Test Methods. Technical report, Federal Rail Administration, Washington D.C., 1982.

[22] V. Kappatos, C. Selcuk, T. H. Gan, and Y. Gharaibeh. Decreasing the influence of dis-

persive wave modes in long-range ultrasonic rail testing using wavelets. *IET Conference Publications*, 2011(581 CP), 2011. doi: 10.1049/cp.2011.0617.

[23] Prasanna Karpur and Orlando J Canelones. Enhancement of Ultrasonic Signals. *Ultrasonics*, 30(6):351–357, 1992.

[24] A. Kish and G. Samavedam. Track Buckling Prevention: Theory, Safety Concepts, and Applications. Technical Report March, Federal Rail Administration, 2013. URL http://files/461/Center-TrackBucklingPrevention.pdf.

[25] Andrew Kish and Wesley Mui. Track Buckling Research. Technical report, John A. Volpe National Transportation Systems Center, 2003. URL https://www.volpe.dot.gov/infrastructure-systems-and-technology/structures-and-dynamics/track-buckling-research.

[26] Philip W. Loveday. Semi-analytical finite element analysis of elastic waveguides subjected to axial loads. *Ultrasonics*, 49(3):298–300, 2009. ISSN 0041624X. doi: 10.1016/j.ultras.2008.10.018. URL http://dx.doi.org/10.1016/j.ultras.2008.10.018.

[27] Gregory C. Luppescu, Alexander J. Dawson, and Jennifer E. Michaels. Dispersive matched filtering of ultrasonic guided waves for improved sparse array damage localization. *AIP Conference Proceedings*, 1706(February), 2016. ISSN 15517616. doi: 10.1063/1.4940480.

[28] R. Mallet, P.J. Mudge, T. Gan, and W. Balachandran. Analysis of Cross-Correlation and Wavelet De-Noising for the Reduction of the Effects of Dispersion in Long-Range Ultrasonic Testing. *Insight – Non-Destructive Testing and Condition Monitoring*, 49 (6):1–24, 2007.

[29] M Mazzotti, A Marzani, I Bartoli, and E Viola. Guided waves dispersion analysis

for prestressed viscoelastic waveguides by means of the SAFE method. *International Journal of Solids and Structures*, 49(18):2359–2372, 2012. ISSN 0020-7683. doi: 10.1016/j.ijsolstr.2012.04.041. URL http://dx.doi.org/10.1016/j.ijsolstr.2012.04.041.

[30] W.S. McErvan and G Born. Preliminary Evaluation of Rail Vibration Techniques for Rail Force Measurements. Technical report, Association of American Railroads Technical Center, Chicago, Illinois, 1980.

[31] Friedrich Moser, Laurence J. Jacobs, and Jianmin Qu. Modeling elastic wave propagation in waveguides with the finite element method. *NDT&E InternationalE International*, 32(4):225–234, 1999. ISSN 09638695. doi: 10.1016/S0963-8695(98)00045-0.

[32] Bill Mosley. Production of long-welded and continuous-welded rail, 2008. URL https://www.railtechnologymagazine.com/Rail-News/production-of-long-welded-and-continuous-welded-rail.

[33] F. D. Murnaghan. Finite Deformations of an Elastic Solid. *American Journal of Mathematics*, 59(2):235, April 1937. ISSN 00029327. doi: 10.2307/2371405.

[34] Claudio Nucera and Francesco Lanza di Scalea. Nondestructive measurement of neutral temperature in continuous welded rails by nonlinear ultrasonic guided waves. *The Journal of the Acoustical Society of America*, 136(5):2561–2574, 2014. ISSN 0001-4966. doi: 10.1121/1.4896463.

[35] Choon Byong Park, Richard D Miller, Jianghai Xia, and Kansas Geological Survey. Imaging dispersion curves of surface waves on multi-channel record. *SEG Expanded Abstracts*, 1998.

[36] Kranthi Peddeti and Sridhar Santhanam. Dispersion curves for Lamb wave propagation in prestressed plates using a semi-analytical finite element analysis. *The Journal of the*

Acoustical Society of America, 143(2):829–840, 2018. ISSN 0001-4966. doi: 10.1121/1.5023335. URL http://dx.doi.org/10.1121/1.5023335.

[37] Seyed Kamran Pedram, Sina Fateri, Lu Gan, Alex Haig, and Keith Thornicroft. Split-spectrum processing technique for SNR enhancement of ultrasonic guided wave. *Ultrasonics*, 83:48–59, 2018. ISSN 0041624X. doi: 10.1016/j.ultras.2017.08.002. URL https://doi.org/10.1016/j.ultras.2017.08.002.

[38] Martin H. Sadd. *Wave Motion and Vibration in Continuous Media*. University of Rhode Island, Department of Mechanical Engineering and Applied Mechanics, 2009. URL https://personal.egr.uri.edu/sadd/mce565/notes.htm.

[39] F. Schopfer, F. Binder, A. Wostehoff, T. Schuster, S. von Ende, S. Foll, and R. Lammering. Accurate determination of dispersion curves of guided waves in plates by applying the matrix pencil method to laser vibrometer measurement data. *CEAS Aeronautical Journal*, 4:61–68, 2013. doi: 10.1007/s13272-012-0055-7.

[40] M. Shamshirsaz, F. Bakhtiari-Nejad, M. Khelghatdoost, and S. Asadi. Analytical and experimental analysis of Lamb wave generation in piezoelectrically driven Timoshenko beam. *Journal of Intelligent Material Systems and Structures*, 26(17):2314–2321, 2015. ISSN 15308138. doi: 10.1177/1045389X14554134.

[41] Malcolm Teasdale and Dave Petley. The Canterbury Earthquake: Images of the distorted railway line, 2010. URL https://blogs.agu.org/landslideblog/files/2010/11/10_10-Canterbury-22.jpg.

[42] D. J. Thompson. Wheel-rail noise generation, part III: Rail vibration. *Journal of Sound and Vibration*, 161(3):412–446, 1993. ISSN 0022460X. doi: 10.1006/jsvi.1993.1084.

[43] Bill Wilson. Another fire destroys nearly 100-year-old railroad

bridge, September 2020. URL https://www.rtands.com/rail-news/another-fire-destroys-nearly-100-year-old-railroad-bridge/.

Appendices

Appendix A

Elementary bar and beam theory derivations

Derivations of some major elementary beam theories are provided, along with the simplifying assumptions which result in inconsistencies compared with the 'exact' solution based on the theory of linear elasticity. The derivations here are based on derivations provided in [12, 19, 38].

A.1 Euler-Bernoulli Beam Theory

Euler-Bernoulli Beam Theory is an elementary beam theory in which rotary inertia and shear deformations are ignored, i.e. transverse deflections dominate the motion. Fig. A.1 depicts a differential element of the beam containing the forces and moments of interest. Note the inclusion of an axial force F_0, used to represent the force caused by internal longitudinal stress such as that found in railroads. $V(x,t)$ represents the shear force, $M(x,t)$ represents the bending moment, ρ is the density of the material, and thus ρA is the mass per unit length of the material.

The Euler-Bernoulli governing equation is obtained by performing a force and moment balance on a differential element and applying some relationships from mechanics of materials.

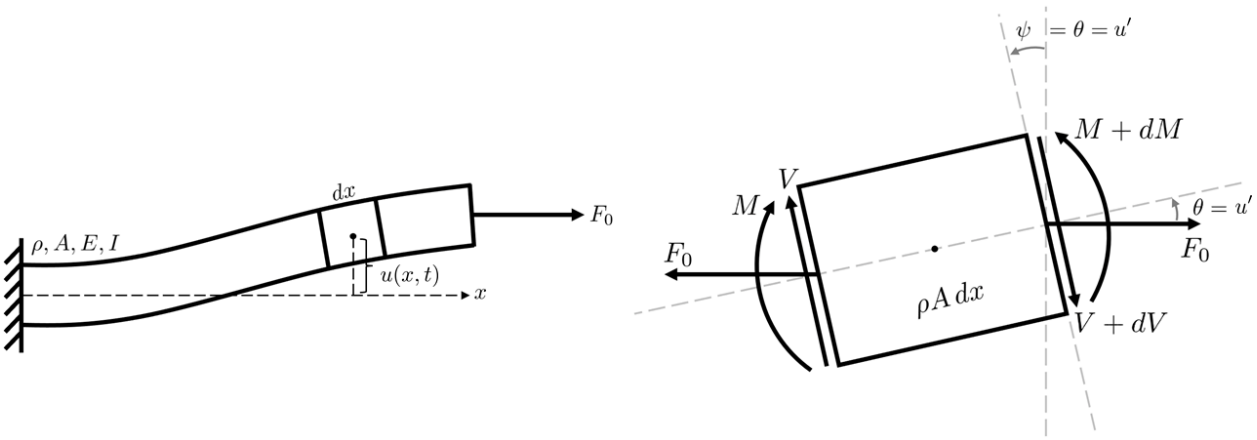

Figure A.1: Euler-Bernoulli beam and a differential element.

Adding up the forces in the transverse direction:

$$\sum F: \qquad V - (V + V'dx) = \rho A\, dx\, \ddot{u}$$

$$\rho A\, \ddot{u} + V' = 0. \tag{A.1}$$

Adding up the moments about the center of the element:

$$\sum M: \qquad -M + (M + M'dx) - V\frac{dx}{2} - (V + V'dx)\frac{dx}{2} - 2(F_0\frac{dx}{2}\sin\theta) = 0$$

Note here that the effect of the axial load is introduced through a nonlinear term, $F_0\frac{dx}{2}\sin\theta$. For small displacements, $\sin\theta \approx \tan\theta = u'$. Thus we can linearize the term for small

displacement, which allows us to simplify the moment balance to

$$M'dx - V\frac{dx}{2} - V\frac{dx}{2} - V'dx\frac{dx}{2} - F_0u'dx = 0$$
$$M' - V - F_0u' = 0$$

$$V = M' - F_0u'. \tag{A.2}$$

From mechanics of materials, the bending moment is proportional to the curvature of the beam by the flexural rigidity EI (assuming a linear elastic response, i.e. Hooke's law). Using some simple geometry, the radius of an osculating circle times the angle provided by the difference in cross-sectional rotation is equal to the arc length between the two cross sections: $d\psi = Rdx$, where $d\psi = \frac{\partial\psi}{\partial x}dx$ is the difference in cross-sectional rotation across a differential element of length dx. Rearranging for the curvature, which is the reciprocal of the radius of the osculating circle, we obtain $\kappa = \psi' dx/dx = \psi'$. Thus the bending moment proportional to the curvature is given by $M(x) = EI\psi'$. In Euler-Bernoulli beam theory, since the cross section remains perpendicular to the central axis of the beam due to the lack of shear deformation, the cross-section rotation angle is identical to the the slope of the beam (linearized for small deflections): $\psi = u'$. Thus the bending moment is related to the transverse deflection by

$$M(x) = EIu'', \tag{A.3}$$

where E is the elastic modulus and I is the moment of inertia.

Differentiating Eq. (A.3) and plugging the result into Eq. (A.2) and subsequently into Eq. (A.1), we obtain the governing equation for an Euler-Bernoulli beam with axial load:

Euler-Bernoulli Beam Theory

$$EI\frac{\partial^4 u}{\partial x^4} + \rho A\frac{\partial^2 u}{\partial t^2} - F_0\frac{\partial^2 u}{\partial x^2} = 0. \tag{A.4}$$

A.1.1 Euler-Bernoulli spectrum relation derivation

The process for solving for the spectrum relation is identical to that shown in Section 2.2, only a bit simpler since Euler-Bernoulli beam theory neglects rotary inertia and shear deformation. Starting with the partial differential equation Eq. (A.4), we apply the separation of variables technique, i.e. we seek a solution of the form

$$u(x,t) = X(x)T(t) = \sum_n \hat{u}_n(x)e^{i\omega_n t}$$

Plugging this into Eq. (A.4), we obtain

$$\begin{aligned}
EI\frac{\partial^4 X(x)}{\partial x^4}T(t) + \rho A\frac{\partial^2 T(t)}{\partial t^2}X(x) - F_0\frac{\partial^2 X(x)}{\partial x^2}T(t) &= 0 \\
EI\frac{\partial^4 X(x)}{\partial x^4} + \rho A\frac{\partial^2 T(t)}{\partial t^2}\frac{X(x)}{T(t)} - F_0\frac{\partial^2 X(x)}{\partial x^2} &= 0 \\
EI\frac{\partial^4 X(x)}{\partial x^4}\frac{1}{X(x)} + \rho A\frac{\partial^2 T(t)}{\partial t^2}\frac{1}{T(t)} - F_0\frac{\partial^2 X(x)}{\partial x^2}\frac{1}{X(x)} &= 0
\end{aligned}$$

$$\frac{EI}{\rho A}\frac{X''''(x)}{X(x)} - \frac{F_0}{\rho A}\frac{X''(x)}{X(x)} = -\frac{\ddot{T}(t)}{T(t)} \qquad = \omega^2$$

Since the left side and the right side both depend on different variables, for equality to hold, they must both be equal to a constant, which with some foresight we select to be ω^2. Thus,

we have two equations, one for the time t and one for the spatial variable x:

$$-\frac{\ddot{T}(t)}{T(t)} = \omega^2 \tag{A.5}$$

$$\frac{EI}{\rho A}\frac{X''''(x)}{X(x)} - \frac{F_0}{\rho A}\frac{X''(x)}{X(x)} = \omega^2 \tag{A.6}$$

First, we solve the first equation for the time component of the solution, $T(t)$, which turns out to be oscillatory:

$$\ddot{T}(t) + \omega^2 T(t) = 0$$

$$T(t) = Re(C_1 e^{i\omega t})$$

where C_1 is a complex number[1].

Now addressing the spatial equation,

$$EIX''''(x) - F_0 X''(x) - \rho A\omega^2 X(x) = 0$$

we can solve this fourth order differential equation using the trial solution

$$X(x) = Re(C_2 e^{-ikt}).$$

Plugging this in yields

$$EIk^4 + F_0 k^2 - \rho A\omega^2 = 0$$

[1]See Appendix A.3 for some insight I have picked up along the way about the use of complex variables, connections with the Fourier Transform, and connections with the Laplace Transform.

which is a quadratic equation for k^2. Solving for the roots of this quadratic equation gives two types of solutions, which are the two spectrum relations for the axially loaded Euler-Bernoulli beam.

$$k_1 = \pm \frac{\sqrt{-F_0 + \sqrt{F_0^2 + 4EI\rho A\omega^2}}}{\sqrt{2EI}}$$
$$k_2 = \mp \frac{\sqrt{-F_0 - \sqrt{F_0^2 + 4EI\rho A\omega^2}}}{\sqrt{2EI}}$$

k_1 is purely real valued and represents the propagating wave mode. Note that it is not a straight line, and as such the phase velocity $c_p = \frac{\omega}{k}$ is not constant; in other words, each frequency has its own propagating velocity. Even when the axial load $F_0 = 0$, the flexural mode is still dispersive. To be clear, dispersion is not a nonlinear effect or to be confused with the acoustoelastic effect relating to nonlinear elasticity. This geometric dispersion, as opposed to material dispersion follows from the provided derivation of Bernoulli-Euler beam theory which assumed a linear elastic material response according to Hooke's law. While the stress dependence comes from a nonlinear geometric term ($F_0 \frac{dx}{2} \sin\theta$), for small displacements this can be linearized, resulting in a linear governing equation.

While k_1 is purely real, k_2 is purely imaginary and corresponds to an evanescent mode. Despite having a somewhat non-intuitive 'imaginary' wavenumber/wavelength, evanescent modes *are* real and physical (contrary to what some authors, such as [38], claim), and correspond to spatially damped vibrations. Mathematically, this is evident because the imaginary wavenumber results in a real valued exponential decay spatial solution, which coupled with the oscillatory time solution gives these 'spatially damped' vibrations. To be clear, there is no damping, i.e. friction or dissipation, in this model; evanescent modes are a purely geometric effect and are necessary for satisfying boundary conditions. In most cases, evanescent modes decay quickly, so they can often be ignored and indeed are ignored in this

thesis; however, the curious reader is encouraged to read further in Doyle [12].

A.2 Timoshenko Beam Theory

While Euler-Bernoulli beam theory is sufficient for low frequencies, at higher frequencies with shorter wavelengths, one can imagine that the assumption that the beam cross section does not have rotary inertia or shear deformations may start to break down. Timoshenko Beam Theory accounts for these effects, and thus provides a more accurate model[2].

In the Euler-Bernoulli beam theory, since cross sections of the beam are required to remain perpendicular to the neutral axis of the beam, their angle (for small displacements) is given by $\frac{\partial u}{\partial x}$ (as in Fig. A.1). In the Timoshenko beam theory, the angle that the cross section makes with the vertical axis is instead treated as an independent variable ψ (as in Fig. A.2); the shear strain is thus given by the difference $\psi - \frac{\partial u}{\partial x}$, i.e. the deviation of the cross-section from perpendicular. The new shear and bending moment are therefore

$$V = -GA\kappa(\frac{\partial u}{\partial x} - \psi) \tag{A.7}$$

$$M = EI\frac{\partial \psi}{\partial x} \tag{A.8}$$

where κ is a constant depending on the cross section called the Timoshenko correction factor and $G = \frac{E}{2(1+\nu)}$ is the shear modulus. In practice, it is best to choose κ to match the high frequency response for the particular use case, be it from experimental data or an 'exact' (3D) theory of elasticity solution, such as Pochhammer-Chree or Rayleigh-Lamb waves. In this work, the general value of $\kappa = (\frac{0.87+1.12\nu}{1+\nu})^2 \approx \frac{\pi^2}{12}$ (which seeks to give good agreement

[2]There is also an intermediate theory developed by Lord Rayleigh known as Rayleigh beam theory, which accounts for rotary effects but *not* shear deformations; however, it does perform as well as Timoshenko beam theory.

with the Lamb wave solution) provided in [12] is sufficient.

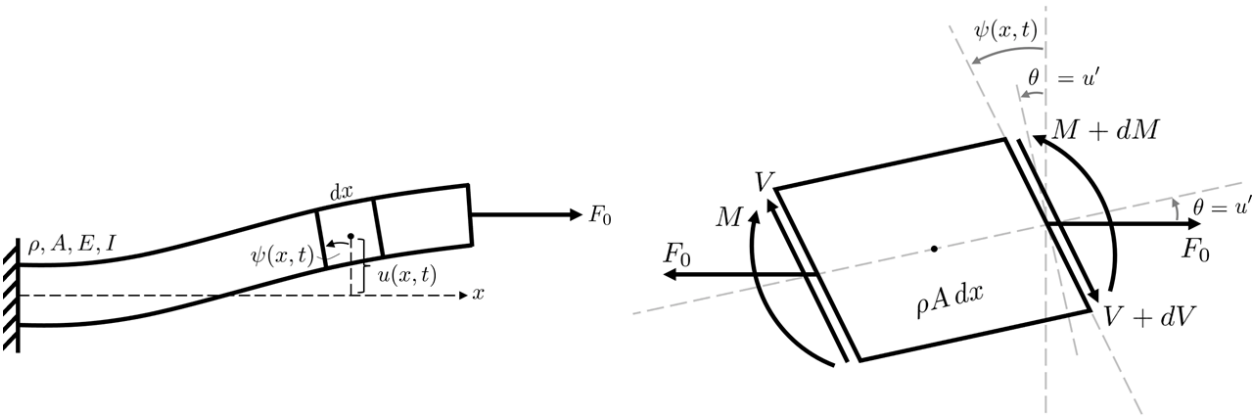

Figure A.2: Timoshenko beam and a differential element.

As in the Euler-Bernoulli case, we will use a simple force and moment balance, combined with the shear and bending moment definitions, to obtain the governing equations. Adding up the forces in the transverse direction on a differential element:

$$\sum F: \qquad V - (V + V'dx) = \rho A dx \ddot{u}$$

$$\rho A \ddot{u} + V' = 0. \tag{A.9}$$

Adding up the moments about the center of the element (and now accounting for the rotary inertia of the element with a non-zero right hand side):

$$\sum M: \qquad -M + (M + M'dx) - V\frac{dx}{2} - (V + V'dx)\frac{dx}{2} - 2(F_0\frac{dx}{2}\sin\theta) = \rho I dx\ddot{\psi}$$

$$M'dx - V\frac{dx}{2} - V\frac{dx}{2} - V'dx\frac{dx}{2} - F_0u'dx = \rho I dx\ddot{\psi}$$

$$M' - V - F_0u' = \rho I\ddot{\psi}$$

$$\rho I\ddot{\psi} - M' + V + F_0u' = 0. \tag{A.10}$$

Now, plugging the shear and moment relations Eq. (A.7) and Eq. (A.8) into the force and moment balances Eq. (A.9) and Eq. (A.10), we can obtain the two coupled Timoshenko Beam governing equations for the transverse displacement v and cross section rotation ψ:

TIMOSHENKO BEAM THEORY

$$\rho A\frac{\partial^2 u}{\partial t^2} - GA\kappa(\frac{\partial^2 u}{\partial x^2} - \frac{\partial \psi}{\partial x}) = 0 \tag{A.11}$$

$$\rho I\frac{\partial^2 \psi}{\partial t^2} - EI\frac{\partial^2 \psi}{\partial x^2} - GA\kappa(\frac{\partial u}{\partial x} - \psi) + F_0\frac{\partial u}{\partial x} = 0 \tag{A.12}$$

A.3 Separation of variables insights

The following section provides some extra insight and background about the solution technique used to form the theoretical foundation of this thesis work. Topics discussed include the interpretation of the separation of variables technique as a Fourier transform, intuition about the spectrum relation as, and connections with other solution techniques such as the Laplace transform.

A.3.1 Fourier transform

The reader may have noticed some notational differences between a traditional separation of variables decomposition $u(x,t) = X(x)T(t)$ such as that used in Appendix A.1 and the decomposition used in Section 2.2. In practice, the temporal solution in vibration and wave propagation problems is typically $T(t) = Re(C_1 e^{i\omega_n t}) = A\cos\omega_n t + B\sin\omega_n t = |C_1|\cos(\omega_n t - \phi)$, where $C_1 = A - Bi$ and $\phi = \arg(C_1) = \arctan\frac{A}{B}$. Furthermore, the circular functions are orthogonal for different values of $\omega_n = \frac{2\pi n}{T}$, i.e.

$$\frac{2}{T}\int_0^T \cos(\omega_n t)cos(\omega_m t) = \begin{cases} 1 & \text{if } m = n \\ 0 & \text{if } m \neq n \end{cases}$$

where T represents the period for a periodic signal. Therefore, the total solution can be a combination of individual vibration solutions at different frequencies, i.e.

$$\begin{aligned} u(x,t) &= X(x)T(t) \\ &= Re(\sum_n \hat{u}_n(x)e^{i\omega_n t}) \end{aligned}$$

It can be shown that if $\hat{u}_n(x)$ are complex conjugate symmetric about the zero frequency, the imaginary components will cancel out, allowing us to drop the $Re(*)$ requirement. In practice, using the FFT algorithm, this equates to the frequency spectrum being complex conjugate mirrored about the Nyquist frequency. With this in mind, the total solution then becomes

$$\begin{aligned} u(x,t) &= X(x)T(t) \\ &= \sum_{n=0}^{N-1} \hat{u}_n(x)e^{i\omega_n t} \end{aligned}$$

which we recognize as the definition of the discrete Fourier transform[3]. Thus, in vibration problems, the separation of variables solution technique in which we assume a solution of the form $Ae^{\lambda t}$ really corresponds to taking a Fourier transform to transform the PDE into a set of ODEs in terms of the Fourier coefficients, which contain the spatial dependence of the solution.

A note on the Laplace transform

An alternative method for solving PDEs is to use the Laplace transform. In the examples in this thesis, the Fourier and Laplace transforms can be used almost interchangeably. The (bilateral) Laplace Transform is defined as

$$F(s) = L(f(t)) = \int_{-\infty}^{\infty} e^{-st} f(t) dt$$

where s represents the complex frequency $s = \sigma + i\omega$. If we restrict the complex frequency to the imaginary axis, i.e. $s = \cancel{\sigma}^{0} + i\omega$, we recover the definition of the Fourier transform:

$$\begin{aligned} \hat{f}(\omega) &= F(f(t)) \\ &= L(f(t))|_{s=i\omega} = F(s)|_{s=i\omega} \\ &= \int_{-\infty}^{\infty} e^{-i\omega t} f(t) dt \end{aligned}$$

Thus the separation of variables solution can also be thought of as evaluating the Laplace transform along the imaginary axis.

So to summarize, when we are interested in solving equations such as beam or string vibration

[3]For details about the discrete vs. continuous Fourier transforms, sampling considerations, algorithmic implementation of the Fourier transform, and other important considerations, Doyle [12] provides a wonderful and thorough review of the topic with helpful graphics and examples.

problems (either for modal analysis or for wave propagation solutions), all of the following methods are related or equivalent to each other:

1. Separation of variables & assuming solutions of the form $Ae^{\lambda t}$
2. Fourier transform
3. Laplace transform

A.3.2 More about the spatially-dependent Fourier coefficients

As shown in Appendix A.3.1, in wave-propagation problems, it is useful and convenient to represent the solution as a separation of variables solution of the form $u(x,t) = \sum \hat{u}_n(x)e^{i\omega_n t}$, which is simply a Fourier decomposition of the solution in terms of its frequency components. For wave propagation problems, we can further interpret the meaning of the Fourier coefficients $\hat{u}_n(x)$. In particular, the Fourier coefficients can be decomposed into an amplitude spectrum $\hat{U}$, which is a property of the propagating wave, and a transfer function (or phase spectrum) $G(x)$, which is a property of the structure:

$$\hat{u}_n(x) = \hat{U}G(x)$$

For the structures considered in this thesis, which have constant geometry and material properties, it can be shown that the transfer function $G(x)$ is, similar to the temporal solution, an exponential of the form $G(x) = e^{-ik_n x}$, where k_n is the wavenumber corresponding to frequency ω_n. Thus the total solution for wave propagation problems typically has the form

$$u(x,t) = \sum_n \hat{U}_n e^{-i(k_n x - \omega_n t)}$$

which is referred to as the 'spectral solution'. The amplitude spectrum $\hat{U}_n = a_n + b_n i \in \mathbb{C}^{n\times 1}$ is a vector of complex numbers at each frequency representing the amplitude and phase of that frequency component. Each component can be plotted in the complex plane as a vector, as depicted in Fig. 2.2; rectangular coordinates correspond to defining the frequency component in terms of the 'amount of sine' and 'amount of cosine', whereas polar coordinates are the more intuitive amplitude/phase description. Applying the transfer function $G(x) = e^{-ik_n x}$ to the Fourier coefficient rotates the phase while keeping the amplitude constant. Thus, wave propagation can be viewed in the frequency-domain as simply rotating the Fourier coefficients around the origin by an amount dependent on the wavenumber k_n.

Depending on the context, using polar or rectangular coordinates may have advantages or disadvantages. For example, in polar coordinates, an issue arises due to the non-uniqueness of angles, resulting in a wrapping every 2π radians; this is not an issue in rectangular coordinates.